Space Sci Rev
DOI 10.1007/s11214-014-0098-7

The Imaging Ultraviolet Spectrograph (IUVS) for the MAVEN Mission

William E. McClintock · Nicholas M. Schneider · Gregory M. Holsclaw · John T. Clarke · Alan C. Hoskins · Ian Stewart · Franck Montmessin · Roger V. Yelle · Justin Deighan

Received: 11 March 2014 / Accepted: 2 September 2014

Abstract The Imaging Ultraviolet Spectrograph (IUVS) is one of nine science instruments aboard the Mars Atmosphere and Volatile and EvolutioN (MAVEN) spacecraft. MAVEN, launched in November 18, 2013 and arriving at Mars in September 2014, is designed to explore the planet's upper atmosphere and ionosphere and examine their interaction with the solar wind and solar ultraviolet radiation. IUVS is one of the most powerful spectrographs sent to another planet, with several key capabilities: (1) separate Far-UV & Mid-UV channels for stray light control, (2) a high resolution echelle mode to resolve deuterium and hydrogen emission, (3) internal instrument pointing and scanning capabilities to allow complete mapping and nearly-continuous operation, and (4) optimization for airglow studies.

Keywords Atmosphere · Exosphere · Mars · MAVEN · Spectrograph · Ultraviolet

1 Introduction

The Imaging Ultraviolet Spectrograph is one of three science instrument suites aboard the Mars Atmosphere and Volatile and EvolutioN spacecraft. MAVEN, which launched on November 18, 2013 and arrives at Mars in September 2014, is designed to explore the planet's upper atmosphere and ionosphere and examine their interaction with the solar wind

W.E. McClintock (✉) · N.M. Schneider · G.M. Holsclaw · A.C. Hoskins · I. Stewart · J. Deighan
Laboratory for Atmospheric and Space Physics, University of Colorado, 1234 Innovation Dr. Boulder,
CO 80303, Boulder, USA
e-mail: william.mcclintock@lasp.colorado.edu

J.T. Clarke
Astronomy Department, Boston University, Boston, MA 02215, USA

F. Montmessin
LATMOS, CNRS, Guyancort, France

R.V. Yelle
Department of Planetary Sciences Lunar & Planetary Laboratory, University of Arizona, Tucson,
AZ 85726, USA

and solar ultraviolet radiation. A goal of the mission is to obtain a comprehensive picture of the current state of the Mars upper atmosphere and ionosphere and the processes that control atmospheric escape. Data returned by MAVEN will allow us to determine the role that loss of volatile species from the atmosphere to space has played in shaping the history of Mars climate, liquid water, and habitability. MAVEN is designed to answer three top-level science questions (Jakowski et al., this issue):

- What is the current state of the upper atmosphere and ionosphere, and what processes control it?
- What are the rates of escape of atmospheric gases to space today and how do they relate to the underlying processes that control the upper atmosphere?
- What has been the total atmosphere loss to space through time?

MAVEN's instrument complement answers these questions by combining observations of Mars' atmosphere and ionosphere with observations of the solar influences that control it. MAVEN has four instruments for atmospheric measurements that record atoms, molecules and ions through *in situ* measurements, probing conditions at the location of the spacecraft as it passes through the upper atmosphere. (See accompanying articles in this issue.) By contrast, IUVS derives atmospheric properties at a distance through spectroscopic measurements of UV emissions of from atmospheric gases. IUVS makes quantitative measurements of the Mars' atmosphere between altitudes of 30 and 4500 km, over all latitudes, longitudes and local times.

Specifically, IUVS measures the composition and structure of the upper atmosphere by measuring:

- Thermosphere vertical profiles of neutrals (H, C, N, O, CO and N_2) and ions (C^+, CO_2^+) using limb scanning.
- Column abundance maps of H, C, N, O, CO_2, O_3 and dust in the upper atmosphere over the portion of the planetary disk that is illuminated and visible from high orbital altitudes using disk mapping.
- Coronal vertical profiles of hot species (H, D and O) using coronal scans.
- Mesosphere/thermosphere vertical profiles of CO_2 and O_3 using stellar occultations.

These observations offer three major contributions to MAVEN science: (1) making independent measurements of key properties also measured by *in situ* instruments for validation and redundancy; (2) providing the global context for *in situ* measurements taken along the spacecraft orbit, and (3) making unique measurements of atmospheric constituents and properties not possible with other instruments. Furthermore, thanks to instrument design and spacecraft accommodation, IUVS can observe Mars nearly continuously throughout the mission. The traceability of MAVEN science objectives to the IUVS investigation described in this paper is summarized in Table 1.

2 IUVS Science Objectives

2.1 Overview

Mars has already been intensely studied at UV wavelengths, first by the Mariner 6, 7 and 9 spacecraft that visited 1969–1972 (Barth 1974; Barth et al. 1972a, 1971; Stewart et al. 1972; Stewart 1972). Then followed observations by four Earth-orbiting telescopes: the Extreme UV Explorer (Krasnopolsky and Gladstone 2005, 1996), Hubble Space Telescope

Table 1 IUVS Science Traceability Matrix

Measurement Requirements	Instrument and Spacecraft Requirements		Science Results	
Global-Scale Composition and Structure	Imaging Ultra-Violet Spectroscopy	Observational Approach	Derived Physical Quantities	Scientific Products
Vertical profiles and column abundances of H, C, N, O, CO, N_2, and CO_2 from the homopause up to two scale heights (∼ 1500 km for coronal H and O, ∼24 km for CO_2) above the exobase with a vertical resolution of one scale height for each species and 25 % precision	115–330 nm wavelength range $\lambda/\Delta\lambda \sim 200$ nominal spectral resolution	Limb viewing to measure species column densities vs. altitude	Column densities and vertical profiles of H, C, N, O, CO, N_2, CO_2, C^+ and CO_2^+	Spatial maps and vertical profiles of the atomic, molecular, and ion properties of the upper atmosphere and ionosphere, including the D/H ratio in the upper atmosphere
	6 km vertical altitude resolution on the limb	Planet mapping from high altitude each orbit	Scale heights, temperatures, and altitudes of the exobase and of the airglow layer peaks	
	200 km horizontal at disk center from apoapsis	Coronal scans to measure the vertical distribution of atoms in the exosphere	D/H ratio	Measurements of the neutral composition and structure of the corona
Vertical profiles and column abundances of C^+ and CO_2^+ from the ionospheric main peak up to the nominal ionopause with one CO_2^+ scale height vertical resolution and 25 % precision		Bi-monthly stellar occultation observation campaigns for low altitude composition and structure		
D/H ratio above the homopause with sufficient precision (∼30 %) to capture spatial/temporal variations (factor of 2) and compare with measured D/H in bulk atmosphere	$\lambda/\Delta\lambda \sim 12000$ nominal spectral resolution			

(Krasnopolsky et al. 1998), the Hopkins Ultraviolet Telescope (Feldman et al. 2000), and the Far UV Spectroscopic Explorer (Krasnopolsky and Feldman 2002, 2001). Most recently Mars has been observed in the UV by the SPICAM instrument on the Mars Express Spacecraft (Bertaux et al. 2006; Leblanc et al. 2006), recently celebrating its tenth year in orbit around Mars, and the Rosetta spacecraft flying by Mars en route to a comet (Feldman et al. 2011). These studies revealed a planet whose ultraviolet spectrum was dominated by emissions caused by the absorption of UV sunlight by carbon dioxide, described in detail by Barth (1974) and Leblanc et al. (2006) and modeled by Fox and Dalgarno (1979). These investigations have identified most or all of the major gases present, along with their excitation mechanisms. As described below, some of the most important findings from the SPICAM observations are the strong variations in the upper atmosphere in composition and structure. Most of these variations remain unexplained due to the lack of observations of causal mechanisms or the limitations of the data themselves. Major questions remain, many of which will be addressed by MAVEN's IUVS.

Mars' atmosphere has been traditionally divided into lower, middle and upper regions, to which we add a higher fourth layer above known as the exosphere or corona. The bottom layer (formally the troposphere) has been extensively studied by prior spacecraft, and is not the focus of the MAVEN mission. IUVS observations are therefore optimized for the three altitude ranges above: the middle atmosphere (∼30–100 km), the upper atmosphere (∼100–225 km), and the corona or exosphere (200–4500 km). While there is some natural division between observing techniques devised for each layer, there are no sharp dividing lines between the layers, and the observations overlap to create a unified picture of the atmosphere. The key science goals for each region are described in the following sections in more detail, along with the critical importance of understanding the coupling between them. We begin with the upper atmosphere, the primary focus of the MAVEN mission, then continue with middle atmosphere that can drive processes from below, and end with the corona, which is supplied by the upper atmosphere.

2.2 Science Goals for Mars Upper Atmosphere (100–225 km)

The upper atmosphere of Mars—more accurately the thermosphere and ionosphere—is primarily controlled by the deposition of EUV solar radiation on the dayside and the subsequent UV radiation. The incident radiation causes instantaneous chemical changes and UV emissions, and also creates and energizes a population of ionospheric electrons, which cause further chemical change and emissions. As with the middle atmosphere, IUVS's first goal is to use these emissions to characterize the structure of upper atmosphere in terms of atomic/ionic composition and temperature. The emissions (and associated physical processes) are known or suspected to be functions of altitude, latitude, longitude, solar zenith angle (SZA) and/or local time, solar activity, distance to the Sun, and Mars season. Crustal magnetic fields are also observed to influence the state of the upper atmosphere, though the controlling mechanisms are not clear. The input of solar EUV energy into the thermosphere creates an extended corona, described in Sect. 2.4. The corona encompasses a flow of escaping atoms, and, perhaps more importantly, a vast low-density cloud of neutrals exposed to a host of escape processes at the edge of space. In this role, processes occurring in the thermosphere are of central importance to the escape of Mars' atmosphere.

FUV and MUV spectra of the upper atmosphere offer great insights into the underlying processes occurring in the thermosphere (Fig. 1). Leblanc et al. (2006) offer a broad review of the field and prior observations while introducing the first in-depth thermospheric results from Mars Express SPICAM. Their Table 1 gives a complete line list with wavelengths

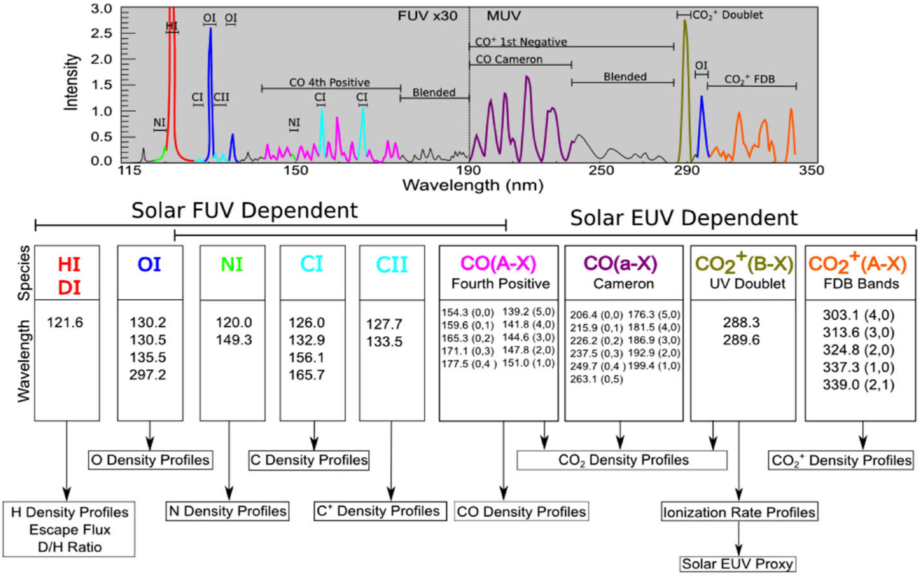

Other potentially observable features include the N_2 V-K band system, CO^+(B-X), and the 131.7nm feature of CO(A-X).
Spectral regions marked in grey are blended emissions and will not by used in pipeline processing.

Fig. 1 Predicted Mars FUV-MUV spectrum and flow down to retrieved quantities

ranges, excitations processes and key references. The major spectral features are atomic lines (H, O and C) and molecular bands (CO_2^+ and CO). While one might naively conclude that nothing could be learned about the primary constituent CO_2, the contrary is actually the case: almost all of the molecular emissions and some of the atomic emissions "may be and probably are produced by action of solar photons and photoelectrons on carbon dioxide" (Barth et al. 1971). This does not imply that little can be learned from the rich spectrum: different chemical and emission processes dominate at different altitudes, and indeed the molecular spectrum is observed to change with altitude (Leblanc et al. 2006). Separation of important driving variables has proven challenging when vertical profiles are obtained through orbital motion, which combines the effects of altitude, SZA and geographic location.

Atmospheric characterization will be accomplished in several ways. At an empirical level, determination of reference altitudes such as the airglow peak will aid in identifying the overall response of the upper atmosphere to perturbations from the middle atmosphere below, and determination of scale heights will reflect temperature conditions responding to heating mechanisms from above. Some composition information can be directly obtained from observed brightnesses (e.g., atomic emissions), and while others will be retrieved from self-consistently modeling of critical photochemical processes with the observed emission profiles (e.g. CO_2 profiles). Critical processes affecting the molecules include ionization, dissociation and excitation, caused by either energetic photons or electrons. Critical processes affecting UV radiation include absorption and emission, plus resonant or fluorescent scattering. These processes are typically coupled together, such as photoionization or electron impact dissociative excitation, with seven major processes in all (see Fig. 2). Once the atmospheric composition and structure are retrieved, atmospheric reference points such as the ionospheric peak and classical exobase can be determined and their variations correlated with driving factors. IUVS scanning capability will prove especially useful in separating

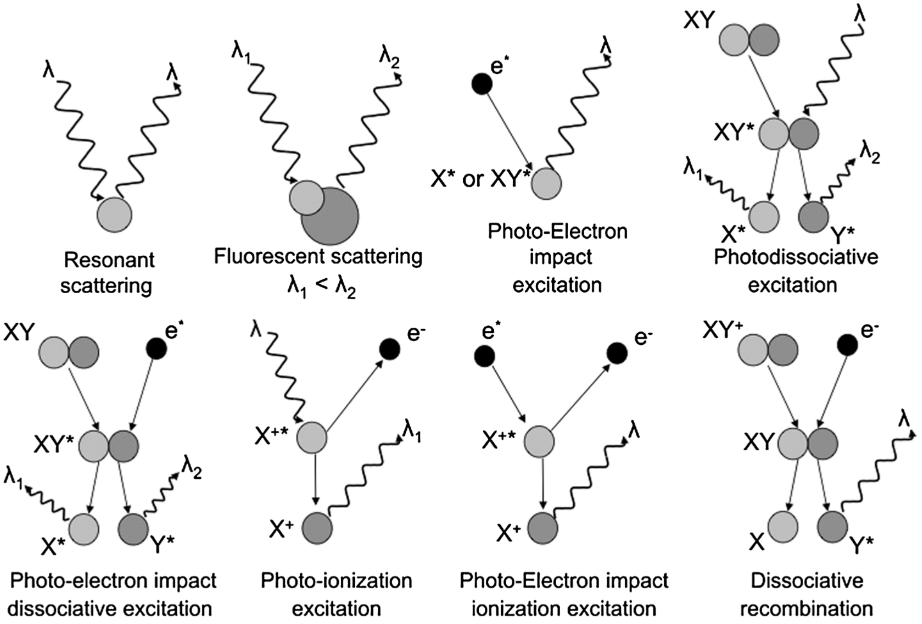

Fig. 2 Schemes of the different mechanisms leading to the dayglow. λ, λ_1 and λ_2 are the wavelength of the incident or emitted photons. X and Y are atoms, and e^- is an electron; X^+ or Y^+ is for a positive ion, and X^*, Y^*, XY^*, or X^{+*} is an atom/molecule/ion in an excited state. From Leblanc et al. (2006)

SZA effects from other variations because it enables the instrument to make a dozen vertical scans as it moves along track during each periapsis pass.

FUV and MUV spectroscopy of the thermosphere and ionosphere are therefore powerful tools for finding composition and structure. Figure 1 highlights how the observed emissions are connected to the atmospheric properties that can be retrieved directly or through modeling. Modeling can also retrieve rates of critical processes which are consistent with the observed emissions, composition and radiation field. Examples include important reaction rates such as the production of O_2^+ and subsequent dissociative recombination leading to hot oxygen escape.

The measured and retrieved properties described above are clearly important for MAVEN's first goal of describing the current state of the Mars atmosphere and the processes that control it. Retrieved properties based on reaction rates and the production of energetic atoms in the upper atmosphere supports MAVEN's second objective of understanding atmospheric escape and its driving processes. In addition to these high-level goals, IUVS will address additional issues. One is confirming that N_2 can be detected in the Vegard-Kaplan band at 276 nm (Leblanc et al. 2007), which adds another constituent for study. Another is the study of auroral emissions near zones of crustal magnetic fields as observed by SPICAM (Bertaux et al. 2005b; Leblanc et al. 2008, 2006)

Thermosphere/ionosphere observations are described further in Sect. 4.1.

2.3 Science Goals for Mars Middle Atmosphere (30–100 km)

The middle atmosphere or mesosphere of Mars lies well below the lowest altitudes MAVEN will reach. But important physical processes occur there which affect the regions MAVEN does visit, impacting the escape processes MAVEN seeks to measure. IUVS is MAVEN's only instrument capable of making measurements of the middle atmosphere and exploring these critical phenomena.

The mesosphere structure is controlled for the most part by the balance between solar heating and radiative cooling, though non-LTE effects have made this a difficult region to study. Perturbations by waves, tides, clouds and hazes further complicate the picture while making it a higher scientific priority. Atmospheric chemistry between minor species has additional effects on composition and vertical transport. For MAVEN purposes, we are especially interested in how spatial and temporal variations in this layer influence the overlying thermosphere and ionosphere. Seasonal effects, both in subsolar latitude and distance from the Sun, will create significant changes in the mesosphere, as will the concomitant changes in dust storms in the lower atmosphere, variable clouds, global circulation and transport. At the most basic level, seasonal changes warm or cool the lower atmosphere, causing a corresponding expansion or contraction of the atmosphere and a raising or lowering of pressure-based reference altitudes. Tides and waves can also carry energy and momentum to the regions overlying the mesosphere.

Atmospheric chemistry in the mesosphere has significant effects on stability and escape. Water and its dissociation products, despite being minor species, play an important role in "repairing" dissociated CO_2 molecules such that their constituent atoms are less susceptible to escape (McElroy and Donahue 1972). These same water products, however, destroy ozone. The HO_x radicals responsible for ozone destruction have never been observed, so it is the absence of ozone, which reveals their presence in the mesosphere. The observed abundance of ozone is highly variable, being highest around the winter pole (Barth and Dick 1974; Perrier et al. 2006) have confirmed that regions of high ozone abundance occur where General Circulation Models (GCM's) predict the absence of water and HO_x radicals. These ozone-rich areas thereby reveal regions where water may be depleted above the mesosphere. The observed seasonal variation in ozone distribution implies a spatially and temporally varying supply of water to the upper atmosphere, and therefore a potential for seasonally-varying escape of hydrogen, oxygen and carbon.

In light of these strong couplings between the mesosphere and layers above, IUVS will undertake multiple types of observation to measure the composition and structure of the middle atmosphere as functions of latitude, longitude, local time/solar zenith angle, and time/season to establish average atmospheric properties. IUVS accomplish these measurements through two primary observation types: stellar occultations and mid-UV imaging of dayside solar reflectance. IUVS may also be capable of measuring and mapping nitric oxide nightglow emissions.

Stellar occultations are a well-established tool for retrieving vertical profiles of density, temperature and composition in Earth and planetary atmospheres. As stars rise or set behind a planet's atmosphere, gases (and aerosols, if present) absorb light with their individual spectroscopic signatures. CO_2 and O_3 are the two gases readily identified in the IUVS wavelength range (Bertaux et al. 2006). Thousands of occultation events have been observed by SPICAM on Mars Express (Montmessin et al. 2006; Quémerais et al. 2006) and vertical profiles have been used to understand and constrain models of the middle atmosphere. To first order the vertical profile can reveal how the mesosphere has been raised, lowered or stretched out by heating or cooling processes. Statistically significant variations in the profiles are evidence of waves, tides or other perturbations. SPICAM results have shown some profiles that exceed saturation vapor pressure for the formation of CO_2 clouds and H_2O ice hazes (Maltagliati et al. 2011). Clouds and hazes can be identified by their bland spectral signatures in the observations; their altitudes and optical depths can be readily deduced from the observations.

MUV mapping is another traditional means of studying planetary mesospheres, providing spatial information instead of vertical profiles. SPICAM observations have shown that ozone and dust can be well mapped, along with MUV surface albedo (Perrier et al. 2006). They further show that these properties vary significantly along a path across the planet, and vary seasonally. These suggestive results make a compelling case for full disk images to complete the global picture.

While most observations require sunlight (or starlight) for illumination or excitation, nightglow allows potentially one more means to study the Mars atmosphere. SPICAM detected significant NO emission bands at 190–270 nm on Mars' nightside, attributing them (as at Venus) to the transport of reactant species carried from the dayside by global circulation (Bertaux et al. 2005a). Where circulation patterns meet and descend on the nightside, increasing densities result in their reaction and the release of UV photons. Although not a mission requirement, IUVS is expected to have the capability to measure and map these emissions whenever observing geometry is favorable, thereby providing constraints on of nightside thermospheric circulation.

Through occultations, MUV mapping and potentially nightglow observations, IUVS measurements will provide the most complete picture to date of the mesosphere. In addition to characterizing the average conditions there, perturbing influences will be identified through their spatial and temporal signatures, allowing a determination of their consequences on the mesosphere and layers above. In addition to serving as observational constraints, the atmospheric baseline and its spatial/temporal variations will also provide input for testing Global Circulation Models of Mars. More information on the nature of the observations in given in Sect. 4.1.

2.4 Science Goals for Mars Corona (Above 200 km)

In the corona, the most important physical processes are the loss of particles to space and the resupply from below (Chamberlain 1963). (While the term *exosphere* usually applies to a physical region of the atmosphere and the *corona* to an observable region, the distinction is not significant in the case of Mars and we use the terms interchangeably.) The corona is important for atmospheric loss through the escaping neutral particles it contains, but also for the target it presents to for numerous other loss processes. In principle the corona has no upper altitude limit, but MAVEN's routine observations only reach the orbit apoapsis of 6200 km. The lower bound occurs at the top of the thermosphere, around 200 km, where collisions between particles start to become important. The most abundant constituents of the corona are H and O atoms. Each is likely to have a thermal component reflecting collisional conditions of the upper thermosphere, and populating what is commonly referred to as a Chamberlain exosphere (Chamberlain 1963). The hydrogen corona has been measured by the Mariner spacecraft (Barth et al. 1972b) and Mars Express (Bertaux et al. 2006; Chaufray et al. 2008). Each of these species may also have a non-thermal component created by other processes. "Hot oxygen", for example, can be created in the thermosphere by dissociative recombination of O_2^+ (Fox and Hać 2014). Depending on the pre- and post-dissociation excitation states, the fragments may have escape energy or enough energy to reach hundreds or thousands of km into the corona. (In this context, "hot" is not meant to imply a high-temperature thermal distribution, only that average energies are well above the background thermal energy.) This process is known as photochemical escape, and it is the leading contender for losing O in proportion to H from H_2O and C from CO_2.

IUVS's primary science goal for coronal observations is quantifying neutral atmospheric escape. Studies of the hydrogen corona have already demonstrated that the loss of hydrogen to space through thermal escape (also known as Jeans escape; Chamberlain 1963) can be highly variable, driven either by dust storms below or other seasonal changes (Chaffin et al. 2014). Routine observation of the H corona at 121.6 nm by IUVS will provide a daily record of H escape over the prime mission, and allow an unambiguous determination of the cause through correlation studies. Hot oxygen has also been detected in a single profile (Feldman et al. 2011), but deriving the escape rate from the shape of the profile is not straightforward. Observations of O at 130.4 nm, especially at altitudes of 1000 km or more will provide stronger constraints on the loss of O due to photochemical escape. Since both hydrogen and oxygen are subject to optical thickness effects in the upper atmosphere and corona, careful modeling will be required to relate coronal brightnesses to densities and escape rates.

Trace amounts of atomic deuterium are also present in the Mars atmosphere and corona, and its abundance relative to atomic hydrogen is a measure of the reservoir of water available to the atmosphere over the life of the planet. As a heavier form of hydrogen, its chemical behavior is nearly identical; but, its higher mass reduces its susceptibility to thermal escape. If substantial amounts of water have been broken down and the hydrogen lost by thermal escape, then the deuterium left behind will become enriched relative to hydrogen. D/H enrichment in the lower Mars atmosphere has been measured at 5.6 (Krasnopolsky et al. 1998), but its value in the corona where loss occurs has not been measured. IUVS will use an echelle mode to spectrally resolve D and H Lyman alpha emission to find the coronal D/H ratio and its dependence on other variables, if any.

MAVEN's coronal observations are described further in Sect. 4.1.

3 Measurement Requirements

The chief goal of the IUVS investigation is to determine the state of the Mars upper atmosphere by measuring the densities of species that populate it and their temperatures. Reference to Fig. 1 indicates that H, D, C, N, O, C^+, CO, CO^+, CO_2^+ and N_2 are present and have emission lines (for the atoms) and bands (for the molecules) that can be measured using an ultraviolet spectrograph working in the 115–350 nm wavelength range. Most of these can be distinguished from one another with a spectral resolution $\lambda/\Delta\lambda \sim 150$–$200$. The exception is H and D whose resonance emission lines have wavelengths of 121.567 nm and 121.534 nm and whose relative intensities are ~200:1, respectively. Unambiguous separation of these two species requires $R \sim 7500$, or better. IUVS uses of limb altitude scanning (Fig. 5), a technique demonstrated by the Ultraviolet Spectrometers aboard the Mariner spacecraft, in order to measure the vertical distribution of these species. Refereeing to Fig. 5b, sampling over at altitude range ~100–220 km with a vertical resolution of ~1 scale height (12 km for CO_2) is adequate for this purpose.

IUVS also measures column densities (total content from top to bottom of the upper atmosphere of important species including H, C, N, O, CO_2, O_3 as well as dust) by mapping the disk at ultraviolet wavelengths near MAVEN orbit apoapsis. These maps provide global context for the limb scans performed near apoapsis. Reference to Fig. 6 indicates that upper atmospheric structures are adequately sampled with spatial resolution of a few degrees in latitude and longitude (aerocentric degrees). We have set, somewhat arbitrarily, the IUVS requirement for spatial resolution in these measurements to be 170 km (3 aerocentric degrees) per image pixel.

Finally, IUVS probes the mesosphere/lower thermosphere using stellar occultations. An ultraviolet spectrometer with wavelength coverage and spectral resolution required for upper atmosphere emission studies is well suited for measuring altitude profiles of CO_2 and

Table 2 IUVS Measurement Requirements

Parameter	Requirement
Wavelength Coverage	
Composition and Structure	120–330 nm
Deuterium-to-Hydrogen	121.1–122.1 nm
Stellar Occultation	125–310 nm
Spectral Resolution	
Composition and Structure	0.6 nm (115–190 nm) and 1.2 nm (180–330 nm)
Deuterium-to-Hydrogen	0.009 nm ($R \sim 13{,}000$)
Stellar Occultation	2.5 nm (115–190 nm) and 5.0 nm (180–330 nm)
Spatial Coverage	
Altitude Range (Limb Scans)	90 km–220 km during periapsis passes
Spatial Resolution	
Thermosphere (Limb Scans)	12 km below 750 km altitude (CO_2 scale height)
Corona (Vertical Scans)	750 km above 750 km altitude (H and O)
Horizontal (Disk Maps)	170 km × 170 km pixel footprint (3° aerocentric pixel)
Stellar Occultation	4 km vertical resolution
Field of View	
Limb Scans	0.176° (3 mrad) × 11.25° (8 spatial elements)
Disk Maps	1.4° × 11.25° (10 spatial elements)
Deuterium-to-Hydrogen	0.057° (1 mrad) × 1.7° (1 spatial element)
Stellar Occultation	>0.6° square
Field of Regard	
Limb Scans	24 × 10 Degrees
Disk Maps	60 × 10 Degrees
Radiometric Sensitivity	
Composition and Structure	[CO], [CO_2^+] 25 % precision, H_{CO}, $H_{CO_2^+}$ 15 % precision in 1 periapsis pass
Deuterium-to-Hydrogen	Measure D intensity to 30 % precision
Stellar Occultation	Top of Atmosphere SNR = 30 for Tint = 2 sec for the brightest stars

O_3, which have variable strength, continuous absorption cross sections in the 115–200 nm and the 200–340 nm wavelength ranges, respectively. Occultations place requirements on spacecraft pointing that are not necessary for emission spectroscopy because the target star must remain steady in instrument field of view during the entire observation in order to obtain an unambiguous measurement.

The IUVS measurement requirements that enable the science goals discussed above are summarized in Table 2. These are met by a small, single-element telescope feeding a plane-grating spectrograph with two observing modes. The first mode (referred to as 'normal mode') provides both broad spectral coverage (120–330 nm) and moderate resolution ($R \sim 200$) to measure global-scale upper-atmosphere composition and structure. The second mode (referred to as 'echelle mode') measures column abundances of D and hydrogen H. This mode has high spectral resolution ($R > 11{,}000$ in order to separate the two emissions by three resolution elements) and only a few nm of spectral coverage.

Fig. 3 IUVS placement on the APP aligns the slit with the APP $\boldsymbol{i}$ axis, the nadir Field-of-Regard with $+\boldsymbol{j}$ and the limb Field-of-Regard with $-\boldsymbol{k}$. By motion of the two-axis gimbal and the scan mirror, which rotates around the $\boldsymbol{i}$ axis, most desired pointings and orientations of the slit can be accomplished. In practice these must be coordinated with other instruments and is subject to spacecraft constraints

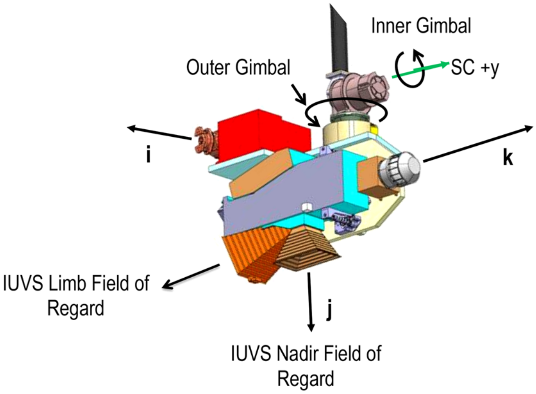

4 Observing Strategy & Data Processing

4.1 IUVS Observing Strategy

After reaching Mars, the MAVEN spacecraft will enter a near-polar orbit with a 75° inclination, a 6250 km apoapsis altitude, a 160 km periapsis altitude, and a 4.5-hour duration. The orbit precesses around the planet due to the combination of gravitational and atmospheric drag effects, allowing a wide variety of viewing and sampling opportunities over the 1-earth-year primary mission.

IUVS observations are organized by orbit phase: periapsis, apoapsis and “orbit sides”. The instrument is mounted to an Articulated Payload Platform (APP), which allows instruments to maintain Mars-pointing while the spacecraft maintains Sun-pointing or other controlled attitudes, as shown in Fig. 3. Both the spacecraft and APP typically change orientation during the transition between orbit phases. IUVS shares the APP with the Neutral Gas and Ion Mass Spectrometer (NGIMS), and SupraThermal And Thermal Ion Composition Experiment (STATIC). Each of these three instruments has specific pointing requirements that are unfavorable for the others, so some observations occur on alternate orbits. IUVS uses a pivoting plane mirror for mapping and scanning that does not affect the other two instruments’ pointing. The scan mirror can also select between two separate fields of regard (FOR) referred to as ‘limb’ and ‘nadir’. The combination of the APP, two FOR’s and the scan mirror allows IUVS to operate with a duty cycle between 50–100 % depending on the orbit-sharing plan with NGIMS and STATIC. The scheduling of observations during periapsis and the orbit sides remains regular for periods of weeks, but changes based on instrument opportunities or limitations and on the spacecraft’s sun-pointing requirements.

IUVS uses a long, narrow slit (11° × 0.06°) in the telescope focal plane to provide entrance to the spectrograph and define the instrument instantaneous field of view (IFOV). At an instant in time, IUVS uses array detectors to record images that contain spectra in one dimension and spatial variations along the slit in the other dimension. Altitude profiles and disk maps are built up by successively displacing the slit perpendicular to its long axis and recording additional spectral-spatial images.

Figure 4 summarizes IUVS observation types during the orbital phases. All three panels show views in the plane of the spacecraft orbit. During apoapsis imaging (A) the APP attitude is held constant with the j’axis parallel the orbit line of apsides. IUVS moves its scan mirror with a whiskbroom motion in order to map the disk of Mars. Coronal scans and D-to-H ratio measurements are performed along the “orbit sides” (B) by pointing the IUVS line

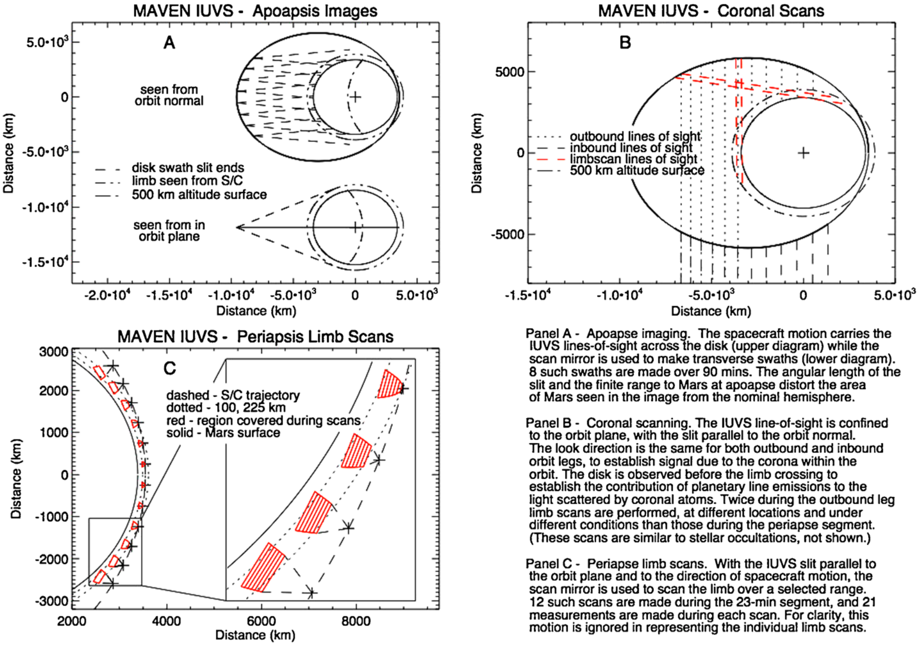

Panel A - Apoapse imaging. The spacecraft motion carries the IUVS lines-of-sight across the disk (upper diagram) while the scan mirror is used to make transverse swaths (lower diagram). 8 such swaths are made over 90 mins. The angular length of the slit and the finite range to Mars at apoapse distort the area of Mars seen in the image from the nominal hemisphere.

Panel B - Coronal scanning. The IUVS line-of-sight is confined to the orbit plane, with the slit parallel to the orbit normal. The look direction is the same for both outbound and inbound orbit legs, to establish signal due to the corona within the orbit. The disk is observed before the limb crossing to establish the contribution of planetary line emissions to the light scattered by coronal atoms. Twice during the outbound leg limb scans are performed, at different locations and under different conditions than those during the periapse segment. (These scans are similar to stellar occultations, not shown.)

Panel C - Periapse limb scans. With the IUVS slit parallel to the orbit plane and to the direction of spacecraft motion, the scan mirror is used to scan the limb over a selected range. 12 such scans are made during the 23-min segment, and 21 measurements are made during each scan. For clarity, this motion is ignored in representing the individual limb scans.

Fig. 4 IUVS observation types: (**a**) Apoapsis imaging. The spacecraft motion carries the IUVS lines-of-sight across the disk (*upper diagram*) while the scan mirror is used to make transverse swaths (*lower diagram*). Eight such swaths are made over 90 minutes. The angular length of the slit and the finite range to Mars at apoapsis distort the area of Mars seen in the image from the nominal hemisphere. (**b**) Coronal scanning. The IUVS line-of-sight is confined to the orbit plane, with the slit parallel to the orbit normal. The look direction is the same for both outbound and inbound orbit legs, to establish the contribution of planetary line emissions to the light scattered by the coronal atoms. Twice during the outbound leg limb scans are performed, at different locations and under different conditions than those during the periapse segment. (These scans are similar to stellar occultations, not shown.) (**c**) Periapse limb scans. With the IUVS slit parallel to the orbit plane and to the direction of spacecraft motion, the scan mirror is used to scan the limb over a selected range. Twelve such scans are made during the 23-minute segment, and 21 measurements are made during each scan. For clarity, this motion is ignored in representing the individual limb scans

of sight points toward the line of apsides with the slit oriented parallel to orbit normal. IUVS points toward the line of apsides on the outbound leg and away from the line of apsides on the inbound leg. Subtracting the latter from the former removes the contribution to signal arising from interplanetary Lyman alpha radiation. During periapsis limb scans (C), the slit is oriented parallel to the orbit plane and to the direction of spacecraft motion. IUVS uses its scan mirror to perform limb-altitude scans approximately perpendicular to the spacecraft velocity vector.

The periapsis orbit phase spans the ∼23 minutes when the spacecraft altitude is less than approximately 500 km. For this period, the spacecraft orients the APP to place its $\boldsymbol{i}$ axis along the spacecraft velocity vector to allow NGIMS to take data in the ram direction. In this part of the orbit IUVS rotates its scan mirror to view the atmosphere through the limb FOR, which is centered on a line in the APP $\boldsymbol{j}$–$\boldsymbol{k}$ plane that is approximately 12° below the $-\boldsymbol{k}$ axis. Small rotations of the scan mirror project the spectrometer slit onto the limb of the planet so that it traverses the 100–220 km altitude range of the daytime atmosphere at a rate of ∼0.1° per second. During this time the instrument detectors acquire images at a cadence

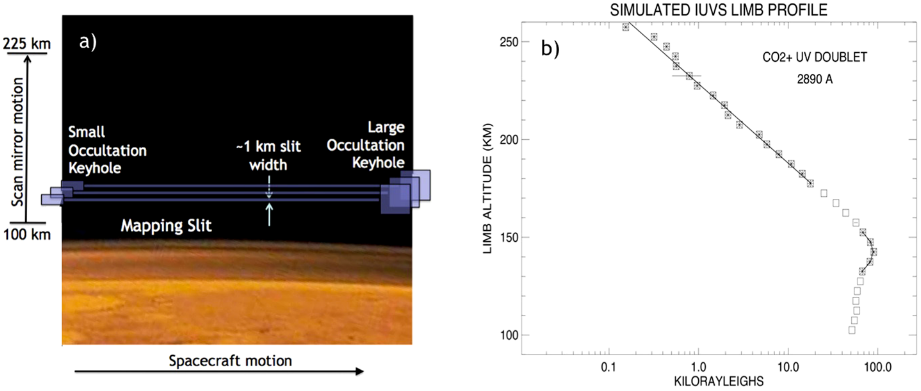

Fig. 5 (**a**) IUVS limb scan geometry and (**b**) resulting data for one emission. Vertical profiles are inverted to yield density from the emission brightnesses and temperature from the slope of the logarithmic profile

of approximately 5 seconds producing ∼5 km smear in altitude sampling (Fig. 5). These are inverted to yield atmospheric densities and temperatures.

When the APP is tracking the spacecraft velocity vector at periapse, the projection of the slit onto the atmosphere is perpendicular to the planet's radius vector at slit center (parallel to the tangent vector at slit center), and altitude above the limb is nearly constant along the slit. (If the center of the slit images at $h = 100$ km, then the curvature of the limb causes the ends of the slit to image $h = 100.5$ km at a slightly larger distance from the spacecraft.) When the APP is tracking the velocity vector while the spacecraft is near the beginning and end of a periapsis pass, the slit can be tilted up to 13° with respect to the horizon. In this case the altitude sampled at one end of the slit is 35 km above the altitude sampled at the other end at any instant in time. Therefore, it is necessary to sum spectra from the detector rows into a number of equally spaced bins along the slit in order to meet the IUVS requirement for 12 km vertical resolution in the limb scans (Table 2).

Near apoapsis the APP is oriented with its $\boldsymbol{i}$ axis perpendicular to the orbit plane and $+\boldsymbol{j}$ parallel to the line of apsides. From this vantage point the disk and extended atmosphere of Mars subtend an angle of ∼45° and IUVS views the planet through its nadir FOR, which is centered on the $+\boldsymbol{j}$ axis. In this case, the combination of spacecraft and scan mirror motion, as illustrated in the lower left panel of Fig. 6, are used to build up images of the disk with ∼160 km resolution (panels b-f). From apoapsis altitude 160 km subtends an angle of ∼1.5° and the required spatial resolution of 160 km along the spacecraft track is obtained by summing spectra into ∼10 equally spaced bins along the slit. The instrument obtains comparable resolution across track by taking approximately 44 exposures while scanning from limb to limb.

The regions of the orbit between apoapsis and periapsis are referred to as the orbit 'sides'. On the outbound side the APP $\boldsymbol{i}$ axis (and therefore the slit) is oriented perpendicular to the spacecraft orbit plane, and the field of view is directed perpendicular to the line of apsides. Here, with the slit perpendicular to the limb, IUVS observes emissions from both the Mars extended atmosphere and from the interplanetary space beyond it. In this orientation it uses both normal incidence and echelle modes to measure hydrogen, deuterium, and hot oxygen. On the inbound side IUVS maintains the same inertial point, which is now outward from the orbit, so that it measures emissions in the same direction observed on the outbound leg. Inbound and outbound are analysed together during ground data processing to characterize the corona along the lines connecting the two sides of the orbit.

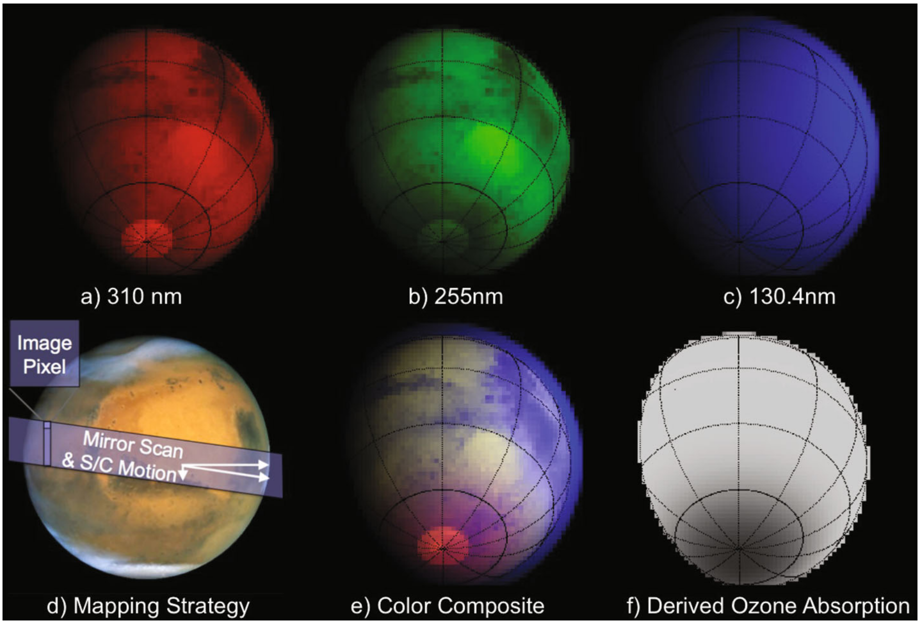

Fig. 6 IUVS disk maps. (**d**) IUVS uses a combination of spacecraft and scan mirror motion to construct global maps of the Mars atmosphere. Images at specific wavelengths are diagnostic of the surface and atmosphere. (**a**) Surface features are evident at 310 nm. (**b**) Attenuation from ozone absorption obscures the polar cap at 255 nm. (**c**) Atomic oxygen in the upper atmosphere can be seen at 130 nm. (**e**) A color composite using the images above combines all these phenomena. (**f**) A ratio of the 255 nm/310 nm images maps ozone absorption

Stellar occultation campaigns will take place every other month to characterize the middle atmosphere on seasonal timescales. Campaigns last for five consecutive orbits, commensurate with one planetary rotation, to give global overage. During these campaigns normal operations are suspended and a combination of spacecraft pointing and APP articulation are used to point the IUVS telescope toward a succession of stars throughout the orbit that maximizes the latitude and local time coverage on the planet. Starlight is imaged into one of the two keyholes, located at the top and bottom of the spectrograph entrance slit (see Figs. 5 and 10), with the remainder of the slit pointed away from the planet in order to minimize spectral contamination. The central region of the slit is too narrow to reliably capture all of the starlight during the course of an occultation in the presence of APP pointing errors and jitter. APP pointing performance and its impacts on keyhole design is discussed in Sect. 5.2.2.

4.2 IUVS Data Processing

IUVS data take the form of two-dimensional images, with one axis in wavelength and the other in spatial location along the slit. Due to stringent limitations on data transmission rates, all MAVEN instruments heavily bin and window their data for downlink. IUVS selects specific wavelength ranges within each detector according to the anticipated spectral features, from dozens to hundreds of bins dependent on observing mode. The spatial dimension is also binned according to expected spatial structure, typically 8–20 bins. In addition to science exposures, IUVS also obtains detector dark frames to remove backgrounds.

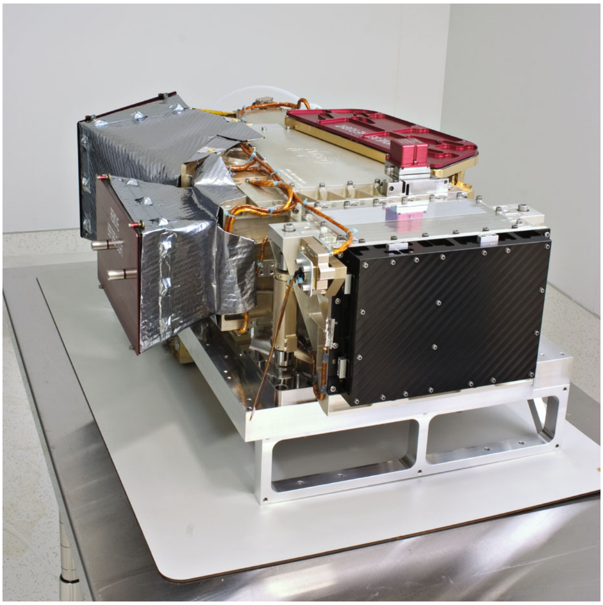

Fig. 7 IUVS instrument image taken during instrument testing at the Laboratory for Atmospheric and Space Physics (LASP) at the University of Colorado. Thermal blankets, fabricated from multi-layer-insulation (MLI) surround the telescope baffles. MLI blankets for the IUVS housing, which are installed before launch are not shown in this image for clarity. Red-tag covers protect the telescope entrance apertures, detector radiator, and an optical alignment cube, which is removed for flight

As data from multiple observing modes are received on the ground, each type is passed to a pipeline for automated scientific processing. First the raw data in measurement units of DNs (data numbers) are corrected for detector dark current, cosmic ray events and other detector backgrounds. Next they are converted to calibrated spectra with units of rayleighs/nm (A rayleigh is a radiance unit equal to 10^6 photons emitted into 4π steradians per second.), and then summed into specific spectral features (in rayleighs) by atomic or molecular species, with observed stray light backgrounds subtracted. The data are gridded in the spatial dimension and map-projected if appropriate. Finally, the reduced data are fed into retrieval algorithms developed for each mode, which derive the relevant physical quantities within the atmosphere such as density, composition and temperature. Each retrieval algorithm employs a "forward model" where atmospheric properties are interactively adjusted until the predicted emission or absorption matches the observations. All data products, from raw data in DN to retrieved quantities in physical units will be archived together in the Atmospheres Node of NASA's Planetary Data System.

5 Instrument Description

5.1 Instrument Overview

IUVS (Fig. 7) is the science instrument component of the MAVEN Remote Sensing (RS) Package that is mounted on the topside of the APP deck. The other component is the Remote Sensing Data Processing Unit (RSDPU), which provides the IUVS electrical interface to the spacecraft and is mounted on the opposite side of the APP deck from IUVS (it is not visible in Fig. 7). An electrical block diagram for the entire RS Package is shown in Fig. 8. Table 3 summarizes the key instrument design parameters. Figure 9 is an optical schematic of IUVS. The corresponding cross-section view through the instrument case in the dispersion plane is shown in Fig. 10.

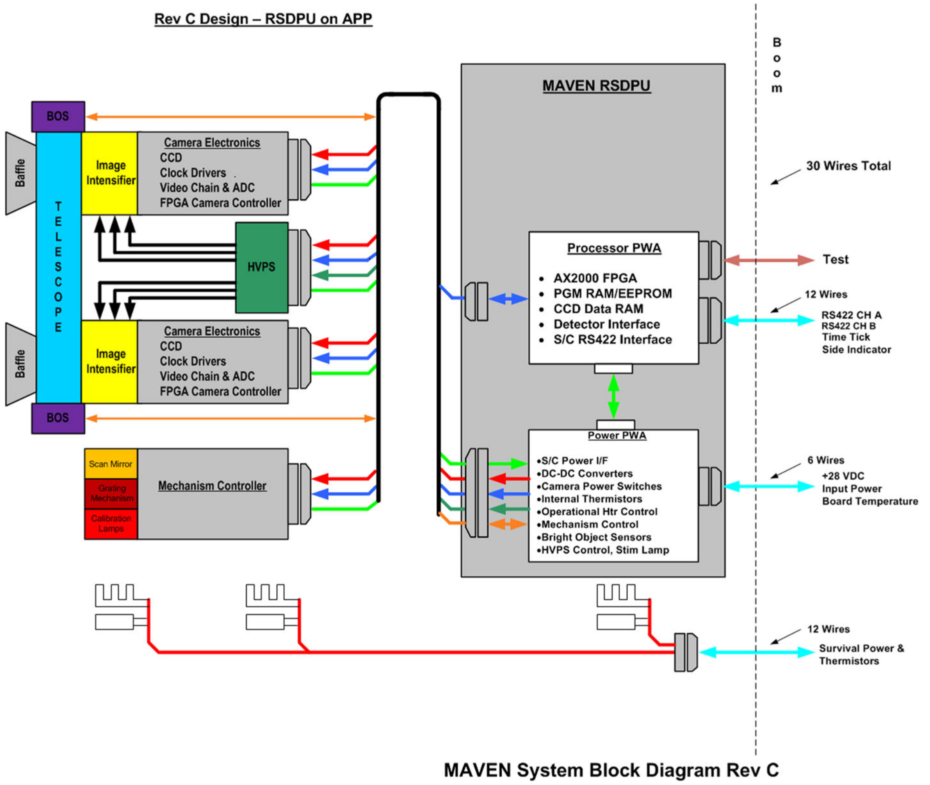

Fig. 8 Remote Sensing Package electrical block diagram. IUVS and RSDPU are mounted on opposite sides of the APP deck

IUVS uses a single, spherical-mirror telescope (T) to image the Mars atmosphere onto the 0.06° × 11° entrance slit (S, Fig. 9) of a plane-grating spectrograph. To enable both altitude profiles and spatial maps the instrument has two independent fields of regard (FOR), one designated as Limb (24° × 11°) and the other designated as Nadir (60° × 11°). These are individually selected by a plane scan mirror (SM) located in front of the telescope. The spectrograph is a modified Czerny-Turner (Czerny and Turner 1930) design equipped with a toroidal camera mirror to eliminate astigmatism at the center of its focal plane. Two separate gratings provide the required resolving powers. One operates near normal incidence and covers 110–340 nm with $R \sim 250$ and the other uses a prism cross-disperser and echelle grating (Harrison 1949; Schroeder 2000) to cover 120–131 nm with $R \sim 19{,}000$.

Black lines in Fig. 9 show the optical path for the normal incidence grating (N). Light enters the spectrograph through the entrance slit (S). It is collimated by a spherical mirror (M1), dispersed by the grating into two diffraction orders (1st order: 180–340 nm and 2nd order: 110–190 nm), and reimaged by a toroidal camera mirror (M2) toward a fused silica, area-division beam splitter (SPT). The beam splitter transmits wavelengths greater than 180 nm to the middle ultraviolet (MUV) detector that includes an image intensifier equipped with a cesium telluride photocathode. Output from the intensifier is coupled to a complementary metal oxide semiconductor (CMOS) array detector by a fiber optic taper. The beam splitter reflects first order and second order light toward the far ultraviolet detector (FUV). FUV is identical to MUV except that its photocathode is cesium iodide. Because cesium io-

Table 3 IUVS instrument design summary

Telescope	
Aperture	13.3 × 20.0 mm
Focal length	100 mm
Field of Regard	
Limb	12.5° × 24°
Nadir	12.5° × 60°
Ultraviolet Spectrograph—Normal Incidence Mode	
Focal length	500 mm
Grating	
Ruling Density	286 groove/mm—blazed at 280 nm(1)
Projected Aperture	66.0 × 100.0 mm
Dispersion	
FUV detector	3.64 nm/mm (2nd order)
MUV detector	7.27 nm/mm (1st order)
Spectral resolution	
FUV detector	0.6 nm
MUV detector	1.2 nm
Wavelength range	
FUV detector	110–190 nm
MUV detector	180–340 nm
Field of View	
Atmosphere	0.06° × 11.3° (0.1 × 19.8 mm slit)
Occultation 1	0.29° × 0.4° (0.5 × 0.7 mm aperture)
Occultation 2	0.69° × 0.9° (1.2 × 1.6 mm aperture)
(1) The grating vendor specification = 276 grooves/mm. The as-delivered = 286 grooves/mm	
Ultraviolet Spectrograph—Echelle Mode	
Focal length	500 mm
Grating	
Ruling Density	44.41 groove/mm—blazed at 69.85°
Projected Aperture	44.6 × 100.0 mm
Cross Disperser	MgF_2 prism—apex angle = 7.5°
Echelle Dispersion	0.031 nm/mm (346th order)
Spectral resolution	14,500
Wavelength range	116–131 nm (362nd order–321st order)
Field of view	0.06° × 1.7° (0.1 × 3.0 mm slit)
Instrument	
Mass	
IUVS	22.1 kg
DPU+Harness	4.7 kg
Average power	
IUVS+RSDPU	28.4 W
Dimensions	
IUVS	61.7 × 54.1 × 23.1 cm^3
RSDPU	25.0 × 32.0 × 9.9 cm^3

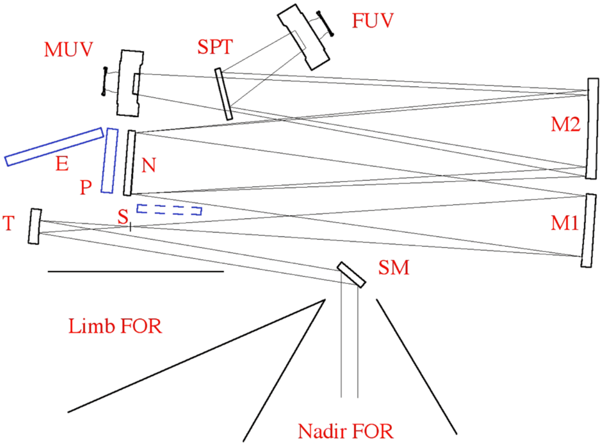

Fig. 9 IUVS optical schematic in the normal-incidence grating configuration. The major optical components are labeled with letters: SM—scan mirror, T—telescope mirror, S—spectrograph entrance slit, M1—spectrograph collimator mirror, N—normal incidence grating, M2—spectrograph camera mirror, SPT—beam splitter, MUV—MUV detector, and FUV—FUV detector. In the echelle configuration, N is rotated clockwise 90° (*blue dashed outline*) placing a prism-echelle grating combination (P-E) in the optical path

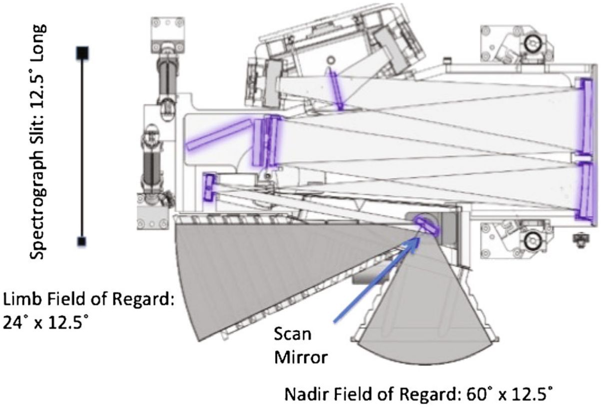

Fig. 10 A cross section through the instrument case in the dispersion plane shows the optical elements, which are highlighted in *purple*, and the optical path, which is shaded with *light grey*. The spectrograph entrance slit, shown on the *left side* of the figure, contains both a narrow, long region (0.06° × 11°) to measure atmospheric emissions and two wider keyholes used for stellar occultations

dide is solar blind (i.e. is very insensitive to photons with wavelengths greater than 200 nm), FUV essentially detects only the second order wavelengths while excluding MUV radiation emitted by the atmosphere and solar continuum radiation reflected from the surface of the planet. A stepper-motor-driven mechanism configures the high resolving power mode by rotating the normal incidence grating approximately 90° (position shown with dashed lines in Fig. 9) out of the collimator beam, illuminating a prism/echelle-grating combination. The FUV detector records the resulting spectrum.

5.2 Nominal Optical Design and Predicted Performance

5.2.1 Spectrograph

Spectral properties of the IUVS are determined from the standard grating equation,

$$n \cdot \lambda = d \cdot \bigl(\sin(\alpha) + \sin(\beta)\bigr) \cdot \cos(\gamma), \tag{1}$$

where α and β are the angles of incidence and diffraction in the dispersion plane (the plane perpendicular to the ruling direction), γ is the angle of an incident ray with respect to the dispersion plane, d is the grating spacing, and n is the order number. Equation (1) can be rearranged in terms of the sum and difference of α and β,

$$n \cdot \lambda = 2 \cdot d \cdot \sin(\theta) \cdot \cos(\phi) \cdot \cos(\gamma), \tag{2}$$

where $\theta = (\alpha + \beta)/2$ and $\phi = (\beta - \alpha)/2$. For IUVS the incidence angle is fixed and the angular dispersion or change in wavelength with change in β is given by

$$\frac{d\lambda}{d\beta} = \frac{d \cdot \cos(\beta) \cdot \cos(\gamma)}{n}. \tag{3}$$

In this configuration the instrument spectral resolution is

$$\Delta\lambda = \frac{d \cdot \cos(\beta) \cdot \cos(\gamma)}{n} \cdot \Delta\beta = \frac{d \cdot \cos(\beta) \cdot \cos(\gamma)}{n} \cdot \frac{\Delta w}{f}, \tag{4}$$

where Δw is the full width at half maximum (FWHM) of the spectrograph slit image in the focal plane convolved with the detector point spread function, and f is the focal length of the camera mirror. Whereas spacing determines the dispersion of a diffraction grating, its blaze angle, θ_B controls its relative efficiency as a function of wavelength

$$E \propto \operatorname{sinc}^2\left[n \cdot \pi \cdot \cos(\beta) \frac{\sin(\theta - \theta_B)}{\sin(\theta)}\right] \tag{5}$$

(Bottema 1981) with a maximum occurring when $\theta = \theta_B$. Equations (1)–(5) along with the selection of detectors govern the design details of the spectrograph.

IUVS employs a pair of imaging detectors each consisting of an image intensifier that has its output optically coupled to a CMOS array detector with a 1024 × 1024 pixel format (Sect. 5.3). Although the detectors have a 24 mm square active area, the optical design is based on a 22 mm square format to provide margin against shifts in instrument alignment caused by launch vibration and changing thermal gradients within the instrument case.

The detectors are identical except that the input photocathode and window are cesium iodide (CsI) and magnesium fluoride (MgF_2), respectively, for the FUV detector and cesium telluride (CsTe) and synthetic silica, respectively, for the MUV detector. The use of CsI for the FUV minimizes the detection of background scattered light from visible and near ultraviolet wavelengths and permits FUV wavelengths to be observed at increased spectral resolution in second order (Hord et al. 1992; McClintock and Lankton 2007; Stewart et al. 1972). This also provides for the compact IUVS focal plane illustrated in Fig. 11. The spectrograph imaging performance is optimized to cover 1st order wavelengths 180–380 nm (90–190 nm in 2nd order) within a 27.5 mm wide by 22 mm tall focal plane. A beam splitter located ∼100 mm in front of the focal plane reflects both 1st and 2nd order toward the FUV detector while transmitting wavelengths >170 nm toward the MUV detector.

The beam splitter was fabricated from a 6 mm-thick Suprasil® 3001 substrate. This material has a sharp spectral cutoff, transmitting >80 % for wavelengths longer than 180 nm and <10 % for wavelengths shorter than 170 nm. This minimizes the amount of second order light that reaches the MUV detector over its nominal 180–340 nm range.

The input side of the beam splitter is coated with equally spaced aluminum strips that are oriented parallel to the grating dispersion direction. These strips, which are 1.5 mm tall and are spaced 2.0 mm apart center-to-center, are covered with a thin MgF_2 coating in order to maximize their reflectivity at FUV wavelengths. A 3:1 reflected-to-transmitted area was

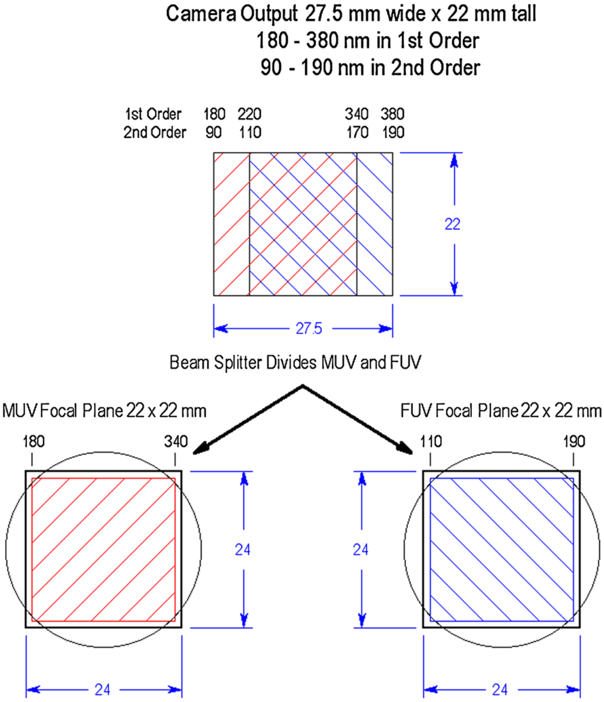

Fig. 11 IUVS focal plane accommodates two detectors using a beam splitter to divide FUV and MUV wavelengths

chosen because MUV emissions from the Mars atmosphere are significantly brighter than FUV emissions.

From a point source in the entrance slit a beam of light that fills the grating is ∼20 mm tall when it reaches the beam splitter, encountering approximately 10 strips as it imaged by the camera mirror toward the focal plane, 100 mm distant. All wavelengths are reflected toward the FUV detector primarily by the aluminized strips (75 % area and ∼80 % reflectance) with a small contribution from the bare substrate (25 % area and ∼4 % reflectance). An anti-reflection coating on the output side of the beam splitter minimizes contamination of the primary image on the MUV detector by secondary reflections (light reflected from the second surface returns to the first surface where it is reflected a second time toward the MUV detector). The ‘picket fence’ structure of the beam splitter forms a coarse grating, with a spacing of 0.5 grooves mm^{-1}. This results in diffraction patterns in the focal plane that are parallel to the slit image and have 80 % of their energy contained within a 0.06 mm tall blur patch or smaller for both detectors. This small degradation in imaging performance along the slit is negligible for the MAVEN IUVS where the minimum spatial resolution element is 2.5 mm (Sect. 4).

We selected a Czerny-Turner configuration for the IUVS design in order to meet the requirements for high spectral resolution in a compact instrument and to support interchangeable gratings with a single set of collimating and imaging optics. A focal length of 500 mm was chosen to maximize spectral dispersion in the echelle mode (see below) within the volume constraints imposed by instrument mounting on the spacecraft APP. Then, the grating and dispersion equations for both the echelle and the normal incidence grating determine the grating designs and remaining spectrograph parameters.

We adopted the standard in-plane ($\gamma = 0$ at the center of the entrance slit) Czerny-Turner configuration with $\beta > \alpha$ for both the normal incidence and echelle gratings. This reduced

Fig. 12 FWHM of the spectrograph-detector point spread function. A nominal first order dispersion of 7.25 nm/mm provides a spectral resolution of ~1.2 nm for MUV and ~0.6 nm for FUV, respectively

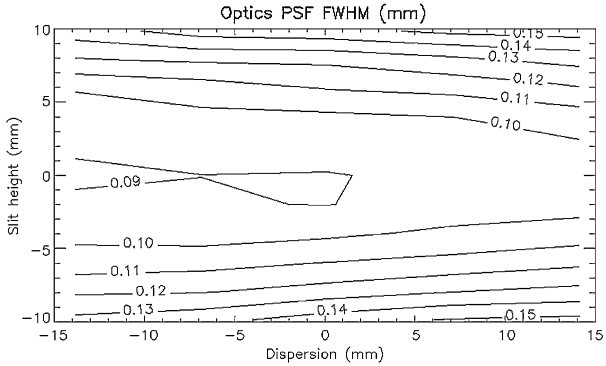

the mechanical packaging complexity associated with accommodating an in-plane mount for the normal incidence and the typical out-of-plane mount for the echelle used for most ground-based spectrographs (Harrison 1949; Schroeder 2000). We also chose to employ a replica of an existing echelle grating, which was manufactured for the Space Telescope Imaging Spectrograph (STIS) (Content et al. 1996), in order to minimize the risk and avoid the cost associated with developing a new echelle grating.

The STIS replica has a ruling density of 44.41 groove/mm ($d = 2\ 2517.5$ nm) and a blaze angle of $\theta_B = 69.85°$. We chose to observe Lyman alpha in order =346 with $\phi = (\beta - \alpha)/2 = 5.95°$. These values maximize the spectrograph response to the deuterium Lyman alpha emission ($\lambda = 121.533$ nm) by placing it at the peak of the echelle blaze function (Eq. (5)) and minimizes the overall size of the optical system in the dispersion direction. Once ϕ is set, Eqs. (1) and (3) determine the normal grating parameters $\alpha = -3.56°$ and $d^{-1} = 276$ grooves/mm. These provide a nominal first order dispersion of 7.25 nm/mm in the spectrograph focal plane.

After the gratings were defined, the spectrograph entrance slit width, camera and collimator mirror angles, and the instrument focal ratio were determined using raytrace analysis to perform a grid search for configurations that maximized optical etendue (the product of entrance pupil area and the solid angle accepted by the system) while meeting the requirements for spectral coverage and resolution listed in Table 2. We used a sphere for the collimator mirror and a toroid for the camera mirror, adjusting the latter's radii of curvature to minimize astigmatism at the center of the field of view. In each case we assumed that the normal incidence grating and the echelle acted as the aperture stop in their respective mode (see Sect. 5.2.2).

We found that we could meet the requirements for the normal incidence mode with a 0.1 mm wide entrance slit and a 66 × 100 mm grating (focal ratios of 7.5 in the dispersion direction and 5.0 in the cross dispersion direction) using a spherical collimator with $R = 1000$ mm and a toroidal camera mirror with $R_x = 1000$ mm and $R_y = 988$ mm. Figure 12 summarizes the predicted imaging performance of the spectrograph-detector system for the entire 27.5 mm wide focal plane of the normal incidence mode using the spectrograph parameters obtained from the grid search.

The system performance was calculated by convolving the optical point spread function (PSF) from the raytrace analysis with the detector PSF, which was modeled as a Gaussian function with a FWHM = 0.05 mm (Sect. 5.3). Results are shown as a contour plot of the FWHM of the system PSF in the spectral dimension. The values were obtained by tracing rays from a 0.1 mm square source located at the entrance slit. A total of 8 equally spaced heights and 5 equally spaced wavelengths were used to cover a 19 mm tall × 27 mm wide focal plane. At each location the spot diagram was binned into 0.01 mm wide pixels and fit with a Gaussian to obtain an estimate of the FWHM of the point spread function for the optical system. These values were then convolved with the detector PSF. This is a convenient metric for imaging performance because 75 % of the enslitted energy of a Gaussian PSF is contained within the FWHM. Values of the FWHM vary from ∼0.12 mm over the central half of the entrance slit to ∼0.16 mm at the top and bottom. This provides slightly better that 0.6 nm resolution and 1.2 nm resolution for FUV and MUV, respectively.

IUVS measures the deuterium and hydrogen Lyman alpha lines (121.533 and 121.567 nm) in order 346 and uses a MgF_2 prism with a 7.5° apex angle as a cross dispersing element to eliminate contamination from adjacent diffraction orders. This arrangement provides a vertical spectral range of 116–131 nm and a free spectral range (the wavelength separation between orders) of 0.35 nm. The 0.54 mm vertical separation between adjacent orders (e.g. 345 and 346) is adequate to support the use of a 3 mm tall spectrograph entrance slit for the echelle mode because the Mars spectrum near the Lyman alpha lines is sparse (Sect. 5.2.3).

The maximum grating size available from the echelle grating vendor (Richardson Laboratories) has a 100 × 100 mm ruled area and its normal projection onto the 66.6 mm wide beam from the spectrograph collimator mirror is 24.5 mm. (The width of the beam intercepted by the echelle is $w \cdot \cos(\alpha) = 44.0$ mm but groove shadowing causes the effective width to be $w \cdot \cos(\beta) = 24.5$ mm (Bottema 1981).) Although this causes a substantial reduction in echelle mode sensitivity, it improves imaging performance. The echelle mode PSF for the optics, calculated from ray tracing, has a FWHM of 0.18 mm. Convolving that with the detector PSF results in an overall system PSF of 0.19 mm (∼8.1 detector pixels), which is equal to a wavelength resolution of 0.006 nm (Eq. (4)). Thus, the deuterium and hydrogen lines are separated by ∼5.6 resolution elements. Also, the entire spectrum from 116–131 nm can be observed without breaks because the free spectral range covers less that half the FUV detector width, varying from 10.5 mm in order 363 for 116 nm to 11.9 mm in order 313 for 131 nm.

5.2.2 *Telescope*

We chose to baseline a single-element for the telescope in order to avoid adding unnecessary optical-mechanical complexity to its design. The entrance slit dimensions and system focal ratio are determined by the spectrograph design and the only undetermined parameter for the telescope is its focal length, which is only constrained by the spatial resolution requirements for the limb scans (12 km) that are acquired when the spacecraft is near periapsis. When the spacecraft altitude is less than 400 km the maximum distance from the instrument to the limb is ∼1500 km. At this distance the minimum telescope focal length required to resolve 12 km with a 0.1 mm wide spectrograph slit is 12.5 mm. We evaluated both a spherical mirror and a segment of a parabola of this size and found that this short focal length is not acceptable because optical aberrations from either design results in a PSF that exceeds 12 km for images at the ends of the 24 mm long slit. Therefore we increased the focal length by trial and error to 100 mm in a somewhat arbitrary compromise between focal length and imaging performance along the slit. Choice of focal length determines the entrance pupil, which is the image of the grating formed by the collimator mirror and telescope, to be a 13.33 mm wide × 20 mm tall mask located 100 mm in front of the telescope.

The 100 mm focal length provides a nominal 0.06° × 11.3° IFOV. Although a parabola produces aberration-free images on the telescope optic axis, we selected a spherical mirror because the parabola's performance relative to a sphere degrades rapidly beyond 3° from

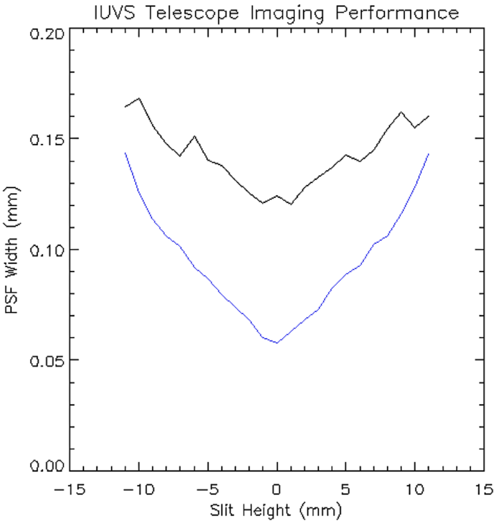

Fig. 13 IUVS telescope imaging performance. The blue curve is a plot of 100 %—geometrical image width, which is contained entirely within the slit for ±7 mm (±4°) from center. The *black curve* shows the effective slit width, which is determined by convolving the telescope PSF with the entrance slit and computing the width containing 80 % of the energy in the image

slit center. Figure 13 summarizes the imaging performance of the telescope for both point sources (stars) and extended sources (the Mars atmosphere). For stars the important metric is the width of the geometric image, which was estimated by tracing rays and determining the maximum width of the spot diagram. The results of the ray trace analysis indicate that the minimum width at best focus is ∼0.06 mm and that the entire geometrical image is contained within the slit over the central region of IFOV (±7 mm from slit center). We convolved the PSF from a point source with a 0.1 mm wide boxcar and used the width containing 80 % of the energy as a metric for the angular resolution for extended sources. In this case the angular width of the IFOV increases from 0.07° at the center of the slit to 0.10° at the ends. This corresponds to 1.65–2.4 km from a range of 1500 km, which is the maximum distance to the limb during periapsis observations. During apoapsis imaging the projected slit width varies from 6.9 km at center to 10 km at the ends. In all cases the projected slit width is much smaller than the required spatial resolution (Table 2) and IUVS will rotate the scan mirror during image acquisition for both periapsis and apoapsis measurements in order to avoid 'picket fence' sampling of the atmosphere.

IUVS performs occultation observations using a combination of its internal scan mirror and the spacecraft APP to place the image of a star in one of two apertures that are located at either end of the atmosphere slit. Early designs incorporated a pair of 1.2 mm wide × 1.5 mm long (0.69° × 0.86°) apertures to accommodate the telescope PSF, which is ∼0.11° for 100 % enslitted energy in the geometrical image, and to accommodate APP accuracy and stability performance, which was specified by the spacecraft designers to be ±0.3° and ±0.25° over 4 minutes, respectively. After the APP was fabricated its measured performance was approximately a factor or 2 better than the original estimates; therefore we reduced the size of one of the apertures to 0.5 mm wide × 0.8 mm tall. The smaller aperture is desirable because it reduces the amount of background light that is present during occultations by the sunlit atmosphere. Replacing only a single aperture was considered to be the prudent decision because the original values are based on measurements of a similar platform, which is flying on the Mars Reconnaissance Orbiter Spacecraft, while the later values are based on ground testing.

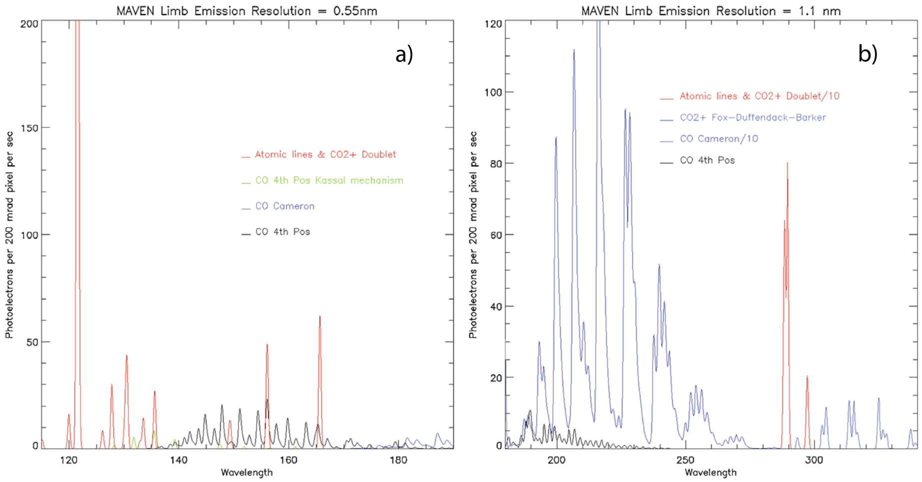

Fig. 14 Simulated normal-mode FUV (*left*) and MUV (*right*) spectra of the Mars airglow as observed during a periapsis limb observation. Emission lines from the major atomic species (H, O, C and N) and from the CO_2^+ are shown in *red*. *Black* and *blue lines* show the 4th positive and Cameron band systems of CO, respectively, as well as the Fox-Duffenback-Barker system of CO_2^+. The observed spectrum is the sum of the atomic and molecular components

5.2.3 Predicted Spectroscopic Performance

During instrument development we constructed instrument models of both the normal and echelle modes using the imaging performance described above and models of the radiometric response curves described in Sect. 6. These were used, along with atmospheric models developed using previous ultraviolet observations (Stewart et al. 1972) to predict the response of the instrument to the Mars atmosphere. Figure 14 shows an example of normal-mode spectra from a periapsis limb observation with a tangent altitude of 110 km, which is the viewing geometry where peak emission from the airglow layer occurs.

At periapsis the image of the entrance slit is parallel to the limb and for each detector we sum all the rows illuminated by the narrow region of the entrance slit to produce a 1024 vector of detector DNs that is plotted as a function of wavelength. In Fig. 14 emission lines from the major atomic species (H, O, C and N) and from CO_2^+ are shown in red. Black and blue lines show the 4th positive and Cameron band systems of CO, respectively, as well as the Fox-Duffenback-Barker system of CO_2^+. The observed spectrum is the sum of the atomic and molecular components.

Whereas detector images in normal mode can easily be decomposed into a series of spectra as a function of location along the spectrograph entrance slit, images in echelle mode are a convolution of spatial and spectral information. The echelle mode covers the 116–131 nm wavelength range. Hopkins Ultraviolet Telescope (Feldman et al. 2000b) observations reveal that the spectrum in this wavelength range is quite sparse. The dominant emission arises from H at 121.567 nm with emission from D at 121.533 nm about 200 times weaker. The major remaining features arise from N (119.955, 120.022 and 120.720 nm), CI (126.155 nm), CII (127.724, 127.751 and 127.755 nm) and O (130.217, 130.486 and 130.603 nm) with an additional weak CO B-X band at 115.2 nm.

Figure 15 shows a simulated echelle image of the Mars atmosphere using the HUT emissions. The image was produced using an optical raytrace program to trace rays from the

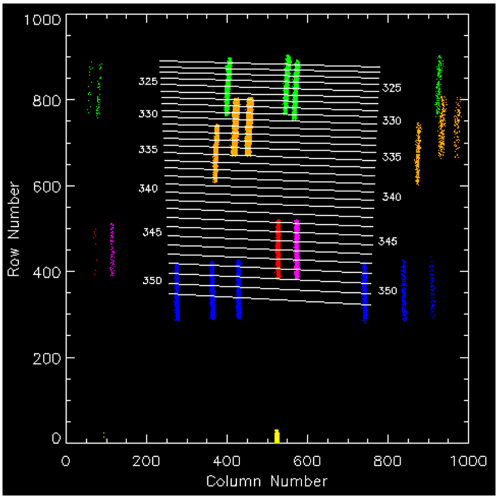

Fig. 15 Simulated echelle image of the Mars atmosphere using the Hut emissions. Color codes are by species with *green* for oxygen, *orange* for carbon, *blue* for nitrogen, *red* for deuterium, and *magenta* for hydrogen. *Dotted lines* show the free spectral range for individual echelle orders for $n = 321$ through $n = 351$

spectrograph entrance slit to the FUV detector. For each of the wavelength listed above 5000 rays, spread randomly over 0.1 mm-wide by 3.0 mm-tall slit, were traced through the system and their positions in the focal plane were recorded as spots. The number of rays in the final focal plane spot diagram was weighted by the echelle grating relative efficiency function (Eq. (5)). This approach accurately simulates both the imaging point spread function and the relative efficiency of the echelle optical system. Because the echelle diffracts into high order numbers a single wavelength may be imaged onto the detector in multiple locations (e.g. HI 121.567 appears in order 346 centered on column 574 and again in order 345 centered on column 115); therefore, each wavelength in the simulation was traced with three separate order numbers. Color codes in Fig. 15 are by species with green for oxygen, orange for carbon, blue for nitrogen, red for deuterium, and magenta for hydrogen. The image of the CO B-X band, which appears in order 365, falls partly beneath the 24 mm^2 active area of the detector. White lines show the locations of the individual echelle orders beginning with 321 toward the top of the detector and ending with 351 at the bottom. The ends of these lines mark the free spectral range of the echelle format (λ at the left side of order n is equal to λ at the right side in order $n - 1$). Their lengths identify the half power points of the echelle efficiency function, which are directly proportional to wavelength. Thus, a continuous echelle spectrum is contained within the free spectral range envelope that lies beneath the half power points of the efficiency function. This is covered in an approximately 500-pixel-wide image on the detector.

5.3 Detector Description

IUVS employs a pair of imaging detectors, each consisting of a Hamamatsu V5180M image intensifier with a 40 mm diameter active area and a Cypress CYIH1SM1000AA-HHCS CMOS array detector. This device is also known as a High Accuracy Star tracker (HAS) and was designed and manufactured by Fill Factory for space-flight applications. It has 0.018 mm square pixels that have well depths of 10^5 electrons (e^-) arranged in a 1024 × 1024 format. Intensifier-CMOS arrays are coupled through a fiber optic with 10 micron input pore spacing that tapers from 24 mm square to 18.44 mm square as shown in Fig. 16.

Each intensifier is equipped with an ultraviolet photocathode, deposited on the interior surface of a 6 mm thick input window, that converts ultraviolet photons to photoelectrons

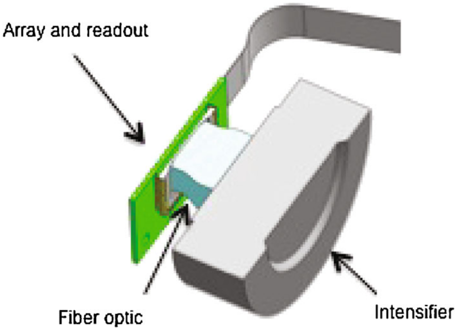

Fig. 16 Each of the two IUVS detectors consists of an image intensifier coupled to a CMOS array detector through a fiber optic taper

with a quantum efficiency that varies from ∼0.01 to ∼0.1 depending on wavelength. The photoelectrons are accelerated through a 40-volt potential and proximity-focused onto the input surface of a microchannel plate (MCP) where they are multiplied. Output electrons from the MCP are further accelerated into a P-43 phosphor by a 6-kilovolt potential producing a localized burst of visible photons (mean wavelength ∼545 nm). Photons from the phosphor output are coupled through the fiber optic taper to the input of the CMOS array where they are detected. During nominal operations voltage is continuously applied to the MCP and phosphor from a high voltage power supply (HVPS), while the voltage between the photocathode and the MCP input is gated on during imaging (+40 volt differential) and gated off (−200 volt differential) during CMOS readout, providing an electronic shutter.

A single photoelectron emanating from the photocathode produces a blur spot in the CMOS output image that has a Gaussian PSF with approximately a 2 pixel (∼0.05 mm after accounting for the taper) FWHM. The radiant gain (output-photons/incident-photon) of the image intensifier can be varied from ∼10 to $\sim 4 \times 10^4$ by adjusting the voltage differential across the MCP from 500 volts to 900 volts. Including ∼50 % fiber loss a single photodetection produces between ∼2.5 and $\sim \times 10^4$ signal electrons in the array, which has a quantum efficiency of ∼0.45 at 545 nm.

Both detectors are housed in a single assembly that includes three electronics boards, which are interconnected by flex circuits. The CMOS chips are mounted on separate small boards, which also contain regulators that provide them power with accurate, stable operating voltages. These are connected to a single larger board that contains a field programmable gate array (FPGA) controller. Control and serial interfaces to the RSDPU are managed through the FPGA. It also generates CMOS clock timing and establishes integration and readout timing. This architecture provides flexibility for windowing (selecting a specific rectangular area of the CMOS for output), and pixel binning (co-adding pixels to reduce data volume and increase signal-to-noise ratio (SNR)).

Each CMOS detector uses 1024 internal amplifiers, one for each column of the array, for readout. There is no global reset for the detector. Both rest and readout are accomplished by simultaneously addressing all pixels in a row, one row at a time. Once a row is addressed for readout, the photo charge in each pixel of that row is latched at the input to its respective column amplifier. The amplifiers are then addressed sequentially and their outputs are digitized by an analog-to-digital converter (ADC) to form a single serial digital data stream. Reading the output of a pixel does not disturb its contents. Reset is accomplished by connecting each pixel to the device drain voltage through a separate gate. This occurs more rapidly than readout because all pixels in a row can be connected simultaneously to the reset line during a single clock cycle.

IUVS uses the CMOS internal analog-to-digital converter in each detector for readout. It is 12 bits deep and its gain is set to 25 e^- per data number (DN—which is the least significant bit produced by the ADC). For the IUVS application, the array is operated in correlated double sampling—nondestructive readout (CDS/NDR). In CDS/NDR mode the array is quickly reset a line at a time. This leaves the pixel array recharged. Immediately after reset, the array is readout, digitized and its 'black' levels stored in an external 1024 × 1024 static random access memory (SRAM), which is located on the detector FPGA controller board. The pixels are not reset after this initial black level readout. After this operation the system collects photoelectrons during an exposure time, Δt_{int}. At the end of the exposure the detector is readout a second time and the black levels are subtracted to retrieve the signals collected during Δt_{int}. This approach eliminates reset noise and pixel-to-pixel variations in the static offset at the expense of increasing the readout noise by $\sqrt{2}$. It also eliminates lag, which is observed in HAS detectors that do not employ CDS/NDR (De Groof et al. 2008). Both the CMOS chip and its output electronics operate at a temperature near −20 °C. This limits the average dark current in the detector to ∼35 e^-/pixel/sec, a factor of 8 below that at room temperature.

The conversion from incident power (photons/sec arriving at the detector input) to output DNs is:

$$DN_{Ph} = \dot{N} \cdot Qe_{Pc} \cdot G_{MCP} \cdot G_{Phosphor} \cdot T_{FOT} \cdot Qe_{CMOS} \cdot G_{ADC} \cdot \Delta t_{int} \tag{6}$$

$$DN_{Ph} = \dot{N} \cdot Qe_{Pc} \cdot G_{Det} \cdot G_{ADC} \cdot \Delta t_{int} \tag{7}$$

$$G_{Det} = G_{MCP} \cdot G_{Phosphor} \cdot T_{FOT} \cdot Qe_{CMOS} \tag{8}$$

$\dot{N}$, Qe_{Pc}, G_{MCP}, $G_{Phosphor}$, T_{FOT}, e_{CMOS}, G_{ADC}, and Δt_{Int} are the photon arrival rate, photocathode quantum efficiency (∼0.1 electrons/photon), MCP gain (electrons/electron), phosphor gain (photons/electron), fiber optic taper transmission, CMOS quantum efficiency (∼0.45 electrons/photon), CMOS analog to digital conversion (0.04 DN/electron), and integration time, respectively. G_{Det} is the average detector amplification (CMOS electrons/photoelectron).

Noise in the IUVS detectors arises from five sources: photon-counting noise, which is equal to the square root of the number of photo-events detected during an integration time; CMOS detector dark current noise, which is equal to the square root of the number of dark charges accumulated during an integration plus read-out time; CMOS detector read noise, which is an average 75 e^- for the IUVS electronics; ADC quantization noise, which is 7 e^- for the HAS analog-to-digital converter; and intensifier 'excess' noise (E). Excess noise results from the statistical nature of the MCP and phosphor gain (Sandel and Broadfoot 1986). For a photon-counting detector, the SNR when detecting N photon events is $\sim\sqrt{N}$. When excess noise is included the SNR is reduced to $\sim\sqrt{N/E}$. Since all the sources produce random noise, the total noise is the root-sum-square of the individual terms and the MAVEN detector SNR when operated in CDS/NDR is given by:

$$SNR = \frac{DN_{Ph}}{\sqrt{G_{ADC} \cdot G_{Det} \cdot E \cdot DN_{Ph} + G_{ADC} \cdot DN_{Dark} + 2 \cdot G_{ADC} \cdot DN_{Read}^2 + 2 \cdot G_{ADC} \cdot DN_{ADC}^2}} \tag{9}$$

where DN_{Dark}, DN_{Read} and DN_{ADC} are the CMOS detector dark signal accumulated during the integration time, pixel read noise, and ADC quantization, respectively. The factor of two accounts for the read noise and digitization noise in the black level image.

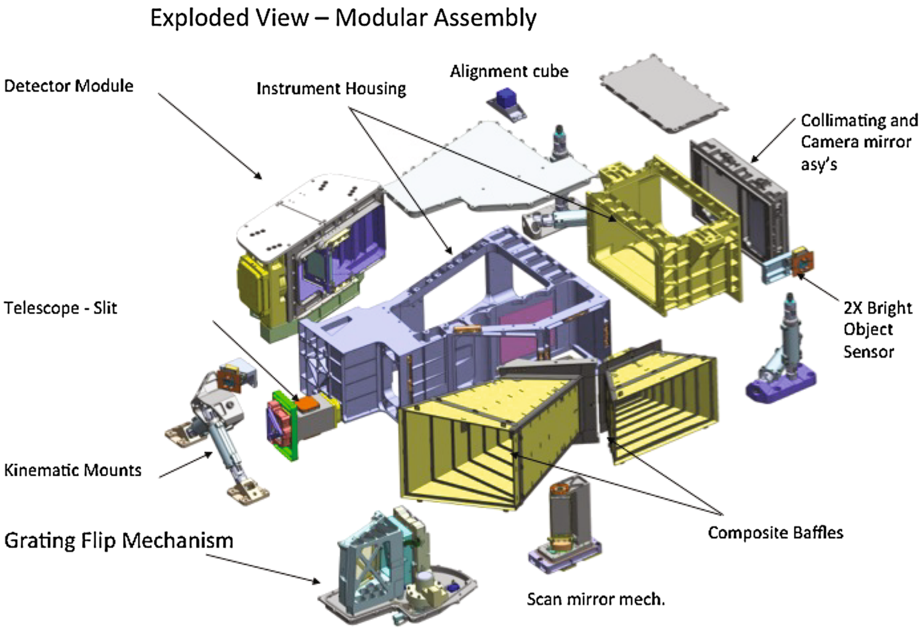

Fig. 17 IUVS consists of a two-piece aluminum structure that supports the detectors and optical-component assemblies

During normal operations, the MCP high voltage is adjusted to provide $\sim 3 \times 10^3$ signal electrons per photo-detection or ~ 120 DN per photo-detection. This greatly exceeds the contributions from dark current noise, electronics read noise, and digitization noise, which have average values of <3 DN (for integrations up to 60 sec), 3 DN, and 0.25 DN, respectively; therefore, the last three terms in the denominator of Eq. (8) may be ignored and the final SNR for each IUVS detector is:

$$SNR \sim [DN_{Ph}/G_{ADC} \cdot G_{Det} \cdot E]^{1/2} = [\dot{N} \cdot Qe_{Pc} \cdot \Delta t_{int}/E]^{1/2} \tag{10}$$

Laboratory measurements indicate that $E \sim 2$ for the IUVS flight intensifiers.

Once an image is readout with its black level subtracted it resides in an external static random access memory located on the detector FPGA printed wire board from which it is transmitted to the RSDPU while a subsequent image is acquired. The detector FPGA supports a large number of windowing and binning schemes that are can be used to tailor the detector data volume to the downlink capability of the spacecraft (Sect. 5.4.3).

5.4 Mechanical Design

Figure 17 is an exploded view of the IUVS, which uses a two-piece 6061-T6 aluminum housing to support the detectors and optical components. These are mounted in modules for ease of assembly and external alignment. Three kinematic mounts (only two are visible in Fig. 17) are used to attach IUVS to the APP, which is a composite structure. The struts dampen vibrational inputs and minimize conducted heat transfer between the APP and IUVS. Their lengths can be adjusted in order to align the IUVS telescope boresight to an optical reference cube mounted on the APP.

Two bright object sensors (BOSs) are also attached to the housing with one aligned to each of the instrument's FORs. Each consists of a Hamamatsu S3590-09 silicon photodiode operated in photovoltaic mode and connected to an operational amplifier operating as a current to voltage converter. The diode is covered by a mask that has an 8.0 mm × 2.5 mm rectangular aperture and is located a 5.4 mm behind a 0.1 mm diameter pinhole. This provides a 72.5° × 26° FOV. The gain of the operational amplifier and the area of the pinhole are designed to produce a >5 volt output if the sun comes within the BOS FOV while MAVEN is in orbit around Mars. This signal is read by the RSDPU and used to safe the instrument scan mirror and turn off high voltage to the detectors in order to prevent permanent damage that would result from sunlight directly entering the spectrograph slit. The BOS system provides a backup for nominal operations where the IUVS uses time-based command sequences to automatically safe itself whenever the sun approaches the FOV. Thus, intervention by the BOS is considered to occur as the result of an anomaly so that high voltage and scan mirror motion can only be reestablished by an external command to IUVS.

The instrument is divided into three optical zones to minimize contamination of the atmospheric signal by sunlight reflected from the surface of the planet. Zone one contains a scan mirror and a pair of optical baffles with extensive vane systems. The second and third zones are the telescope module and the spectrograph, respectively. The spectrograph contains a pair of light traps, one located near the focal plane that intercepts zero order from the normal-incidence grating, and one located just behind the entrance slit that intercepts light scattered from the walls of the telescope cavity. Internal surfaces of all three zones are coated with AnoBlack Cr (Anoplate Inc., Syracuse NY), which consists of two thin layers (∼0.01 mm thick) of electroless nickel. The first layer has large phosphor content. The second has less phosphor and is photoetched to produce a surface that has reduced reflectance.

5.4.1 Scan Mirror and Baffles

The scan mirror that directs the field of view (IFOV) to either the nadir-viewing FOR or to the limb-viewing FOR is located approximately 300 mm in front of the telescope. It is required to direct the instrument's IFOV onto the Mars atmosphere with an internal position accuracy and stability of better than 20 % of the instrument's IFOV width, which is 1.0 milliradians (0.057°), and an angular resolution (minimum step size) of 0.5 milliradians.

The mirror enclosure and the baffle systems for the two FORs are designed so that only the scan mirror directly illuminates the telescope when IUVS views the limb. (When IUVS views Mars through the nadir FOR parts of the telescope mirror are illuminated by a small portion of the walls of the scan mirror enclosure. These are blackened and recessed so that they are not directly illuminated by the external scene. Scatter from starlight illuminating the baffles through either FOR is completely negligible.)

The scan mirror assembly, which is shown in Fig. 18, consists of a titanium housing supporting a mirror spindle, drive motor, and optical angular position encoder. Its total angular range of travel is 120°. The mirror, which is fabricated from BK-7 glass for compatibility with its titanium mount, is bonded into a bezel ring that attaches to a spindle. The spindle is supported on top by a radial bearing and on the bottom by a duplex pair of angular contact bearings. An angular encoder and limited angle brushless DC torque motor procured from Aeroflex are also attached to the bottom of the spindle. The FPGA that is located on the processor board in the RSDPU uses signals generated by the encoder to control the angular position of the scan mirror in increments of 2.75 millidegrees (16-bit resolution over 180°) so that a single mirror step moves the instrument IFOV by 10 % of its width.

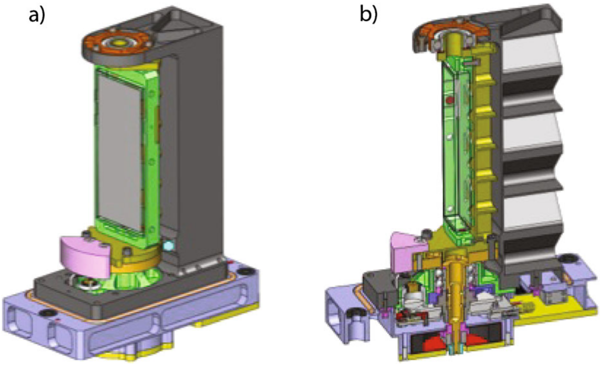

Fig. 18 Isometric and cutaway views of the scan mirror assembly

The semi-custom optical encoder, which was procured from Designed Motion Components, uses a 44.5 mm diameter rotating glass encoder and fixed reticules with light-emitting-diode (LED)/phototransistor pairs to generate and sense fringe patterns. It produces 4096 cycles per full revolution, which is 1.533 milliradians (0.088°) per cycle. The (LED)/phototransistor pairs produce two sinusoidal signals (A and B) that are 90° out of phase. These are digitized to 14 bits resolution and used to compute both a coarse position and a fine position. The average output of the phototransistor is monitored by the RSDPU and can be adjusted by changing the current flow through the LED. This mitigates possible changes in encoder performance due to LED aging during the mission.

To determine coarse position the A and B signals are input to a pair of comparators that each output '1' whenever the input is greater than zero and '0' whenever the input is less than 0. This results in a pair of clock signals that have 50 % duty cycle and are out of phase with each other by 90°. When these two signals are used as input to exclusive or (XOR) logic the output voltage has transitions with a period of 0.383 milliradians (0.022°) that are used to increment or decrement and up-down counter that maintains the coarse count position.

Because the digitized A and B signals closely approximate a sine/cosine pair, they can be used as input to a Coordinate Rotation Digital Computer (CORDIC) algorithm (Volder 1959) in order to calculate a high resolution (fine) encoder position. The CORDIC function implemented in the IUVS encoder produces an output angle as an 18-bit signed integer. Using the upper 6 bits of this result divides one full cycle (0.088°) into 64 intervals, allowing the interpolation of scan mirror coarse position to $1.533/64 = 23.95$ microradians (1.38 millidegrees). The FPGA combines 13 bits from the coarse counter with 6 bits from the CORDIC algorithm to produce a 17-bit scan mirror position (0–180°) with 1.38 millidegree encoder step size (resolution) that is used in the scan mirror control loop.

In addition to the A and B tracks, the encoder disk includes an index channel that provides a zero reference. It consists of a single narrow opening in an opaque track on the disk and an LED/phototransistor pair. Output from the phototransistor, which spikes when the opening passes beneath it, is input to a comparator to generate a narrow pulse that is used during power-up to position the encoder to a known reference angle (fiducial). Subsequent scan mirror angles are measured relative to the fiducial and instantaneous (current) position is determined to within 1.38 milliradians by counting encoder steps.

The FPGA in the RSDPU controls scan mirror position using a proportional-integral-differential (PID) algorithm that operates with a 250-microsecond loop time. Motion is initiated by inputting a 16-bit position command to the control loop, which generates a motor drive voltage that is proportional to the difference between the current mirror position and the commanded position. Thus, a limb scan or a disk map (Sect. 4) is comprised of a series

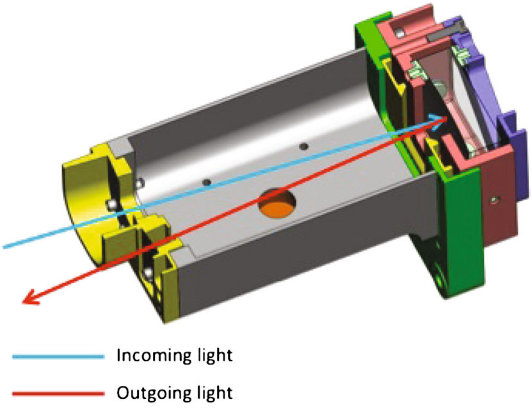

Fig. 19 Cross section view of the telescope assembly

of commands to the mirror input that increment or decrement position as appropriate. The time required to complete a rotation depends on the range to be traveled. Slews over many degrees occur at the rate of 20° per second. During both limb scans and disk maps the rate of motion is typically $\leq 0.1°$ per second and the commanded step size (~ 12 encoder steps) is set to move the IFOV approximately 50 % of its width. In these cases, the scan mirror can step and settle to a new position in approximately 0.05 seconds with an average step-to-step accuracy of better than $\sim\pm 1.5$ encoder steps (~ 12 % of the IFOV).

5.4.2 Telescope Assembly

Figure 19 shows a cross section view of the telescope assembly. Light from the scan mirror enters through the entrance pupil, which is located 100 mm in front of the mirror. It is focused on the onto the spectrograph entrance slit. The pupil and slit are the only optical apertures in the assembly. This helps to minimize the illumination of the telescope walls by stray light originating in the scan mirror cavity.

The telescope mirror is mounted in a cell that attaches to one end of the assembly. It is held in focus by springs that register the spherical imaging surface against three domed brass pads that are located to directly oppose the springs. Two pads on the side and one pad on the bottom and their opposing springs maintain the lateral position of the mirror. Changing the thickness of shims that are underneath the pads provides six degrees of freedom to adjust position, tip and tilt.

5.4.3 Spectrograph

The two-piece instrument housing (see Fig. 17) provides the main structure for the spectrograph case, which supports assemblies containing the optical elements and detectors. All optical elements are held in position by opposing springs and pads, similar to the approach used to position the telescope. Both the collimating and camera mirrors are mounted in a single housing that attaches to the rear of the spectrograph housing. This removable housing provides easy access to both mirrors for alignment and focus. It attaches to the case using an o-ring seal to eliminate light leaks into the spectrograph.

The spectrograph has two operational modes, one employing a low-groove-density (276 grooves/mm) plane grating to provide a resolution $R \sim 200$–300, depending on wavelength and a second employing a cross-dispersing prism and an echelle grating to provide

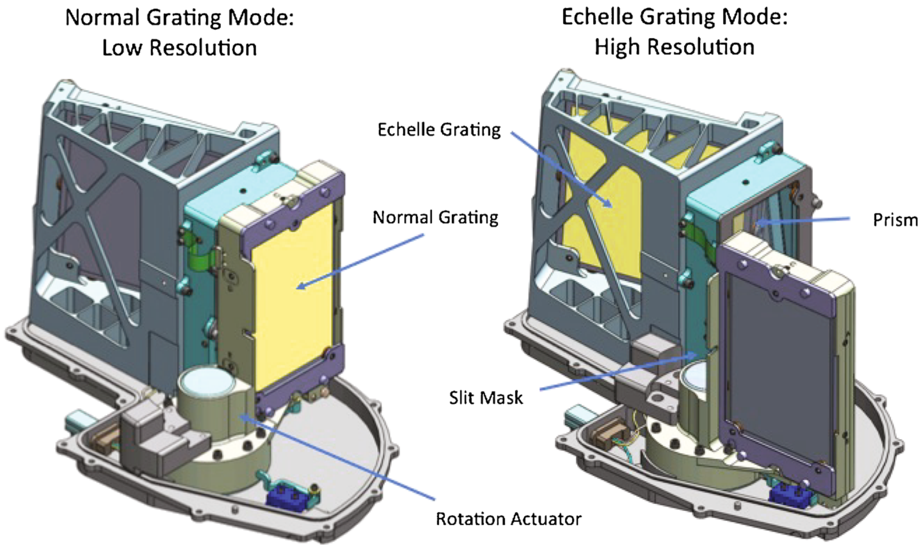

Fig. 20 The *left panel* shows the position of the grating flip mechanism (GFM) for the low-resolution mode. The GFM rotates the normal grating and its housing clockwise approximately 90° in order to illuminate the cross dispersing prism and echelle grating (*right panel*). When the GFM is positioned for echelle mode a mask mounted on the side of the normal grating housing limits the height of the spectrograph entrance slit to be 3 mm tall

$R \sim 12{,}500$. A grating flip mechanism (GFM) rotates the normal-incidence grating and its housing through an angle of 84.6° in order to switch between these two modes. The left panel of Fig. 20 shows the configuration of the GFM in the low-resolution mode. A stepper motor equipped with a planetary gear system that has a 49:1 ratio provides the rotational motion with a resolution of 0.037° per step. The motor is coupled to the bearing system that supports the normal-incidence housing through a torsionally compliant flexure. The GFM changes modes by commanding the motor through 2303 steps in either direction to drive the grating housing against two hard stops on the GFM body that are located ~100 mm from the center of rotation of the grating and its housing. There is no position feedback in the GFM except for limit switches at either end of travel and registration against a hard stop is achieved by commanding a few extra steps to wind up the flexure so that it acts like a spring that forces the housing against the stop. Mechanical detents hold the housing in place once power is removed from the motor. Based on previous experience with this method of registration, the repeatability for positioning the housing against the stop is ±0.025 mm, which corresponds to an angular reproducibility of ±0.25 milliradians (±0.014°). Therefore, a command from low resolution to echelle and back again can cause a shift of up 0.25 mm in the location of the spectrum at the detectors.

Figure 21 shows the detector module, which is a single housing that contains a beam splitter, the detectors with their associated electronics, and a miniature mercury Penray® lamp, procured from UVP, an Analytik Jena Company. The entire module can be removed from the spectrograph structure as a unit, which facilitates assembly and optical alignment. Light from the camera mirror first encounters the beam splitter, which contains 31 aluminized rectangles that are 1.5 mm tall × 57 mm wide and that have a 2 mm center-to-center spacing (see Sect. 5.2.1). Approximately 57 % (75 % from the aluminized strips and 4 % from

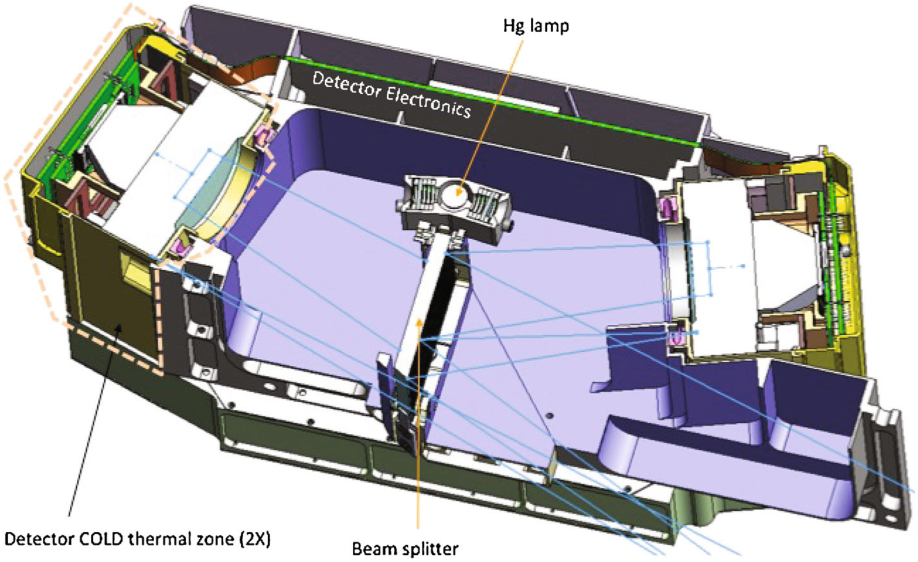

Fig. 21 The detector module includes a housing that supports a beam splitter, the FUV and MUV detector assemblies and a mercury stimulus lamp. A high voltage power supply, not visible in the figure, is attached to the bottom of the housing

the uncoated area) of the light incident on the beam splitter is reflected toward the FUV detector. Light incident on the uncoated areas is transmitted to the MUV detector.

The FUV and MUV detector housings, which each contain a Hamamatsu V5180M image intensifier and a fiber optic taper with 10 micron pore spacing that has a windowless Cypress CYIH1SM1000AA-HHCS CMOS array bonded directly to its output surface. A compression flexure registers the input surface of the taper against the output surface of the intensifier to maintain spatial resolution across the interface between intensifier phosphor and CMOS input.

A 61 mm × 81 mm printed wiring board (PWB), which is soldered to the 84 pins of the j-lead ceramic chip carrier that encloses the CMOS array, provides both electrical connection and mechanical support for the chip. The PWB is fastened to the fiber optic mounting bracket to form an integrated module, which is registered to the output of the intensifier with a copper-beryllium flexure. Six titanium struts are used to mount each detector housing to the module. These provide six degrees of freedom for detector independent alignment and focus and serve to thermally isolate the detectors from the rest of the instrument.

Electrical connection to the CMOS arrays is made through a pair of ridged-flex circuits to a single, 152 mm wide × 127 mm tall, detector-control board (DCB), which contains an RTAX2000 field programmable gate array (FPGA) that operates both detectors simultaneously, performing all required binning/windowing and data compression. In addition to the FPGA, the DCB holds a pair of 2 M × 12 bit SRAM (one for each detector), which are used to perform double correlated sampling, and a pair of 1 M × 1 bit electrically erasable programmable read-only memory (EEPROM) that are used to store a bad pixel map for each detector. After the RSDPU configures the detector FPGA by specifying the number of images, the imaging mode and windowing/binning configurations (Sect. 5.3), and the integration time, the detector operates autonomously until the number of requested images with the specified windowing/binning have been transmitted to a buffer in the RSDPU.

Once an imaging sequence is initiated by the RSDPU the DCB FPGA controls all subsequent timing and data transfer until the sequence is complete. Both single detector and dual detector operation are supported. Two serial low voltage differential signaling (LVDS) ports located on the DCB provide communications with the RSDPU. One operates asynchronously at 57.6 Kbits/sec for the command and configuration interface. The other operates synchronously at 5 Mbits/sec for data transfer to the RSDPU data buffer, which can hold up to seven full frame images from each detector.

A single image begins with a 1-msec detector reset, followed by a 230-msec-long readout of a black level image, which is stored in one side of the $2\ \text{M} \times 12$ SRAM. Next, the detector FPGA issues an 'open shutter' command to the RSDPU. At the end of the integration time the detector FPGA reads out the array replacing each stored black level value in the SRAM with the just-read value minus the stored black level. If both FUV and MUV images have been requested by the RSDPU, these steps occur simultaneously in the two detectors. While data are read into the first side of SRAM, the previously recorded image is transferred to the RSDPU data buffer from the second side of SRAM. Removal of bad pixels, windowing and binning, and data compression are performed on the fly during the transfer using 16-bit wide words. Although the detector FPGA initiates a shutter open command for the two detectors simultaneously, the RSDPU controls the 'shutter close' timing independently for each. This enables different FUV and MUV integration times. The CMOS detector output is digitized to 12 bits. If more that 16 pixels are co-added while forming a binned word for transmission there is a potential for overflow. This is addressed by using a 26-bit wide summing register. After summation the 26 bits are reduced to 16 using a pseudo-logarithmic algorithm in which the 12 bits following the first '1' in the summed value are used as the mantissa and the exponent is ones-complement of the 4 bit representation of the number of leading '0's in the summed value.

A HVPS designed by Battel Engineering, is attached to the bottom of the detector module, and provides the voltages required to operate the FUV and MUV image intensifiers independently. These include fixed -6000 V biases for the phosphors (relative to their respective MCP output voltages) and variable voltages in the range 200–1000 V for the MCP input voltage. The HVPS also applies one of two fixed voltages between the intensifier photocathode, which is located on the inside of the intensifier input window, and the input of the MCP providing an electronic shutter. When the photocathode is held at $+40$ V relative to the MCP photoelectrons are accelerated into it producing a cascades of electrons. When the photocathode is held at -200 V relative to the MCP no acceleration occurs and no cascades occur.

A low-pressure cold cathode mercury gas lamp, produced by Penray®, is attached to the top of the beam splitter housing. Its principal ultraviolet emissions are two atomic lines that are located at 184.9 nm and 253.7 nm. These are isolated for the FUV and MUV detectors, respectively, using passband filters made by Princeton Instruments. The lamp is used for end-to-end (detector-instrument-spacecraft-ground system) testing when it is not practical to use the instrument optical system. It is also used for tracking any spectral 'imprinting' that may take place during operations around Mars.

5.5 Thermal Subsystem

The CMOS arrays in the IUVS detectors operate at temperatures near $-20°$ in order to minimize the effects of dark current noise in the IUVS data (see Fig. 21). This is accommodated by the thermal subsystem using two temperature zones because maintaining the entire instrument at these temperatures using passive techniques requires an unrealistically

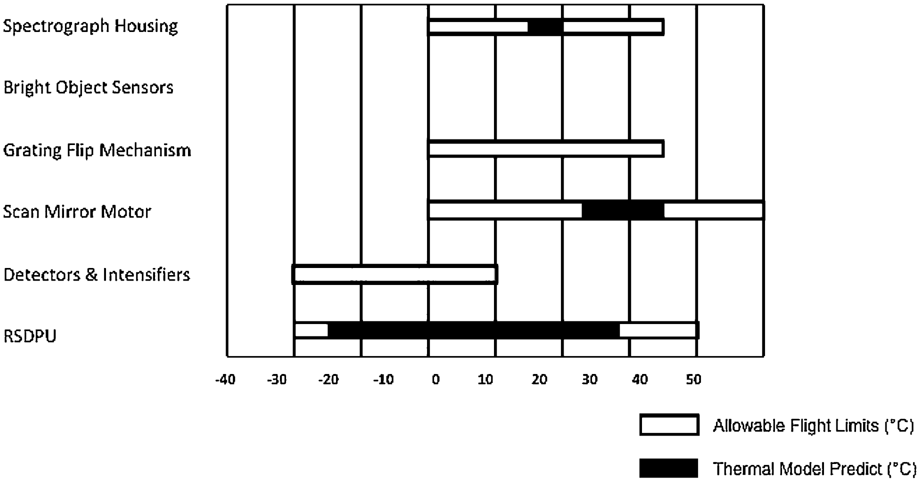

Fig. 22 Predicted performance of the thermal subsystem

large radiator. Using a second thermal zone that is maintained near room temperature for the optics and structure also simplifies alignment, focus, and optical testing. A third thermal zone was implemented for RSDPU thermal control because it can tolerate a wider range of temperature and is physically isolated from IUVS.

IUVS and the RSDPU are thermally isolated from the APP using titanium struts and G10 fiberglass spacers, respectively to achieve a power transfer across the mechanical interfaces to <0.05 W/°C for each component. Titanium mounting flexures were also used to reduce the conduction between the telescope baffles and the instrument housing to <0.05 W/°C. Both IUVS and RSDPU are entirely enclosed in thermal blankets except for the input apertures of the IUVS baffles.

The thermal subsystem uses radiators attached to the instrument case, detector housing, and RSDPU housing to reduce the temperatures to less than the desired minimum operating values. A single radiator attached to the top of the detector housing cools a pair of units (FUV and MUV) each containing an intensifier, fiber taper, CMOS array, and read electronics. The telescope apertures provide radiators for the telescope and scan mirror assemblies. In addition three small radiators are attached to the top of the spectrograph housing at the front, middle and back. A radiator is attached to the top of the RSDPU housing. The RSDPU monitors the temperatures of the three zones and controls them by turning on and off operational heaters to maintain values within high and low limits that are uploaded by ground command.

Thermal models were used to determine radiator and heater sizes and placements. Heat loads into the instrument and radiator view factors were obtained from detailed spacecraft models for the entire mission and include orbital geometry, spacecraft attitude, and APP orientation. The goals for the design were to maintain detector temperatures at 0 °C or lower in order to control dark current and to minimize diurnal temperature variations in the spectrograph in order to minimize wavelength shifts caused by changing thermal gradients within the case. Figure 22 summarizes the predicted performance of the thermal subsystem over the nominal mission life. Temperature ranges shown in Fig. 22 include both diurnal and seasonal variations. For IUVS diurnal thermal variations dominate seasonal variations but these are still less than ±3° for all components. Detector temperatures are expected to range between −25°C and −20 °C. This will limit the dark current to 0.25 DN/sec. For RSDPU the magnitude of the seasonal variations is ∼35 °C with additional ±5 °C diurnal variations. This is acceptable because the RDSPU contains no mechanisms or optical components and the resulting range is well within the operating specifications for the electronic parts.

5.6 Data Processing Unit

The RSDPU is the electrical interface between the IUVS and spacecraft and provides the power and drivers required to operate the IUVS detectors and mechanisms. It is enclosed in a 25.0 × 32.0 × 9.9 cm^3 aluminum box that is attached APP interface plate on the opposite side from the IUVS. The RSDPU contains a pair of PWBs referred to as the power board and processor board, respectively.

The processor board is built around an RTAX2000 FPGA that contains an embedded 8051 microcontroller core (Core8051) supplied by Actel Corporation. In addition to providing the command and data interface to the spacecraft, which operates asynchronously at 57.6 Kbps over an RS-422 serial link, the FPGA controls all of the subsystems within the IUVS. These include:

- Independent command and control of each detector high voltage power supply (HVPS) for, HVPS power on/off, intensifier phosphor voltage on/off, high voltage level for the MCPs, and photocathode shutter open/close
- Actuation of the grating flip mechanism
- Operation of the detector stimulus lamp
- Operation of the scan mirror including the implementation of the PID algorithm used to position the mirror
- Control of the instrument's heaters
- Collection of housekeeping data including various voltages, temperatures, and configuration monitors (e.g. grating flip position)
- Configuration of image windowing and binning
- Storage of images, including a ping pong buffer capable of storing up to 14 full frame images from each detector.

The processor board also supports two 128 K × 8 SRAMS for storage and execution of system code and for microprocessor data memory as well as a 128 K × 8 EEPROM for non-volatile storage of program code. This enables the RSDPU to execute both immediate commands received over the spacecraft interface and stored sequences of commands.

The RSDPU power board contains a low voltage power supply that converts +28-volt spacecraft power to the various voltages required to operate the IUVS subassemblies. These include ±15 v, +5 v, +5.6 v, +3.9 v, and +2.2 v. All subassemblies receive power directly from the power board, which also transmits control signals from the processor board to the HVPS for setting MCP high voltage and adjusts the current flow through the scan mirror LED. These functions are enabled by digital to analog converters (DACs) on the power board. The power board also houses the drive circuits for the scan mirror and grating flip motors, switches for spacecraft power to the heaters, the analog-to-digital converter (ADC) used to sample and digitize sine and cosine voltages from the scan mirror encoder, instrument housekeeping voltages, and temperatures.

6 Measurement Performance

During instrument design we used models to predict its measurement performance, including imaging, spectral resolution, and radiometric sensitivity. These were based on raytrace analysis, measurement of component performance at LASP (detector imaging, dark current, read noise, intensifier gain and photocathode quantum efficiency) and vendor specifications (grating efficiency, mirror reflectivity, and beam splitter transmission). The performance characteristics of the instrument, including radiometric sensitivity, were also measured both before and after instrument environmental test and qualification. Any important differences between modeled and measured performance are noted below.

6.1 Conversion of Instrument Data Numbers to Geophysical Units

IUVS measures the radiance arriving at the entrance pupil of the instrument from the Mars atmosphere, and Eq. (11) defines the conversion of instrument output (data numbers) to geophysical data (radiance or reflectance):

$$L(\lambda_j, \theta_k) = \frac{[DN(\lambda_j, \theta_k) \cdot N(DN(\lambda_j, \theta_k)) - DN_{Dark}(\lambda_j, \theta_k) - S_l(\lambda_j, \theta_k)]/\Delta t}{A \cdot \Delta\lambda \cdot \Omega(\theta_k) \cdot R(\lambda_j, \theta_k)} \tag{11}$$

Here DN is the detector data number output for signal accumulated during integration time Δt in a single pixel with index j, k associated with wavelength (λ_j) and angular position along the spectrograph entrance slit (θ_k). N is the detector linearity correction. DN_{Dark} is the pixel data number resulting from dark charge collected during Δt. A is the area of the entrance pupil, $\Delta\lambda$ is the spectral passband of the spectrograph for a single pixel, and R is the instrument responsivity for pixel j, k. S_l is a stray plus scattered light correction $(S_l = S_l' + S_{Stray})$. S_l is positive for bright spectral features (more light is scattered out of pixel j, k than is scattered in by all other wavelengths), and negative for faint spectral features (less light is scattered out of pixel j, k than is scattered in from all other wavelengths). S_{Stray} represents the light that is diffusely scattered from internal instrument surfaces. $\Omega(\theta_k) = w(\theta_k) \cdot h_{pix} \cdot F_{Tel}^{-2}$ is the solid angle subtended by an aperture defined by the height of a pixel and the width of the spectrograph entrance slit for position θ_k. $R = T_{Optics} \cdot Qe_{Pc} \cdot G_{Det} \cdot G_{ADC}$ is the product of the optics transmission, detector photocathode efficiency, and the detector gain stages.

Detector dark current will be measured by periodically closing the detector electronic shutter throughout each orbit. Nonlinearity is caused by well saturation in the CMOS detectors and by differential nonlinearity in the analog-to-digital converter. It was characterized during detector calibrations before launch. The scattered light correction also appears in the numerator as a value that must be subtracted from observed signal to correct for light scattered from all other wavelengths into position/pixel j, k: $S_l'(\lambda_j, \theta_k) = A \cdot \Delta\lambda \cdot \Omega(\theta_k) \cdot \int L(\lambda') \cdot R(\lambda', \theta_k) \cdot G(\lambda_j - \lambda') d\lambda'$, where G is the grating scatter distribution function (GSDF), which is often approximated as a Lorentzian profile plus constant background (Woods et al. 1994). Pre-launch values for the various parameters appearing in Eq. (11) were determined during instrument characterization and calibration using both radiance and source standards. Radiometric calibrations using radiance standards (irradiance standards and reflectance screens) that fill the instrument aperture and FOV measure the quantity $A \cdot \Delta\lambda \cdot R(\lambda_j, \theta_k) \cdot \Omega(\theta_k)$. Calibrations using standard detectors and star sources that fill only the aperture measure $A \cdot R(\lambda_j, \theta_k)$, and $\Omega(\lambda_j)$ and $\Delta\lambda$ must be determined separately by scanning the FOV and measuring monochromatic lines, respectively. After launch observations of stars during cruise provide measurements of $A \cdot R(\lambda_j, \theta_k) \cdot \Delta\lambda$ that will be accurate to ~10 % (Snow et al. 2013). No specific requirements were placed on S_{Stray}, which is bookkept in the constant term of the GSDF and was not independently characterized before instrument assembly. Instead, the sum of the constant term plus S_{Stray} was determined during instrument calibration. This was accomplished for the FUV channel during vacuum testing by measuring the residual signal at wavelengths less than the short wavelength cutoff it MgF_2 window (<115 nm) and for the MUV channel during ambient testing by measuring the residual signal at wavelengths less than the air cutoff (<180 nm).

6.2 Characterization and Preliminary Calibration Results

6.2.1 As-built Optical Configuration

There were two significant modifications to the IUVS optical configuration during development. The first occurred late in the development when we discovered that the ruling density of the delivered normal incidence gratings from the manufacturer was 286 lines mm^{-1} instead of the 276 lines mm^{-1} that was specified in the purchase order. This led to ∼4 % increase in dispersion that has no significant impact on performance.

The second occurred early in the development when we discovered that approximately 5 % of the zero order beam from the normal incidence grating impinged upon the collimator mirror. If the initial design were retained the collimator would focus this light back onto the grating to form an image of the entrance slit. The grating would then diffract the light from this image toward the camera mirror, which would project an out-of-focus a secondary spectrum onto the detectors. This problem was solved by increasing the normal grating opening angle and repositioning the camera mirror. While this approach had a negligible impact on normal incidence mode performance, it significantly altered the efficiency function of the echelle (Eq. (5)), shifting deuterium Lyman alpha away from the blaze peak. The measured as-built opening angle to the center of the FUV detector for the echelle was 13.32°, placing 121.37 nm at the blaze peak and reducing strength of the deuterium Lyman alpha emission to 0.65 relative to the blaze peak. Because the free spectral range of the echelle spectrum is <12 mm (Sect. 5.2.1) the loss in sensitivity was partially mitigated by reducing the echelle opening angle to 12.74° so that the echelle pattern to covers only one half of the FUV detector. In this configuration the strength of the deuterium emission relative to blaze peak is increased to 0.85.

6.2.2 Detector Characteristics

Intensifier Gain Equation (11) describes the relationship between $L(\lambda_j, \theta_k)$, the radiance at the IUVS entrance pupil, and $DN(\lambda_j, \theta_k)$, the data numbers readout from the detector after an integration time Δt. $DN(\lambda_j, \theta_k)$ is directly proportional to the gain of the MCP in the image intensifier (Eqs. (6)–(8)), which can be adjusted by varying the voltage applied across the MCP input and output surfaces. Typical gain values for the MCPs in the IUVS intensifiers (Hamamatsu V5180M) range between 1 and 1000 for voltages between 500 and 900 volts.

Relative gains for the flight intensifier MCPs were measured over the 400–650 volt range before the intensifiers were installed in the instrument. After installation the gains were characterized by comparing the response to spectral lines of different strengths while varying the integration time and voltage. This allowed us to measure the entire 400–900 volt range. Figure 23 shows the relative voltage-gain curves for both MUV and FUV obtained from those calibrations. We were only able to determine the relative gain because no independent measurements were made for the rest of the detector components, which include photocathode quantum efficiency, phosphor gain, fiber-optic taper transmission, and HAS detector quantum efficiency (Eqs. (6)–(8)). The results shown in Fig. 23 have been normalized so that

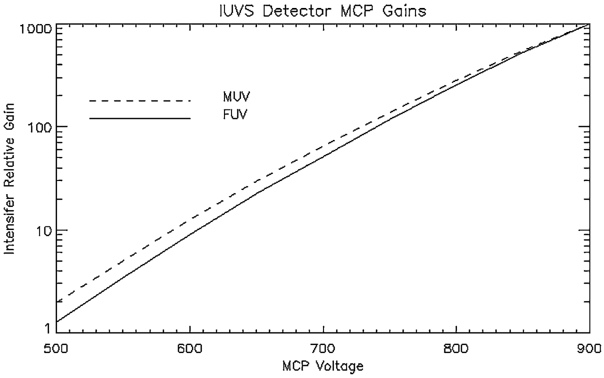

Fig. 23 Relative intensifier MCP gain as function of applied voltage. The two curves have been normalized to $G = 1000$ for $V = 900$ volts

$G_{MCP} = 1000$ for $V = 900$ volts in order to be consistent with nominal values published in the Hamahatsu image intensifier catalog.

In addition to measuring the MCP relative gain, we calculated the product of $G_{Det} * G_{ADC}$, which is the number of output DNs per photoelectron produced by the photocathode, from estimated values of the remaining parameters in Eqs. (6)–(8) using published values from the component manufacturers. These are phosphor gain ($G_{Phos} = 70$) from Hamamatsu, CMOS detector quantum efficiency (0.45) and ADC gain (25 e^-/DN) from the HAS specification data sheet. For the fiber-optic transmission we assumed that it has a bulk transmission (including reflection losses at the input and output) of 0.8 and that the numerical aperture is 0.4, resulting in a transmission of 0.32. Inserting these values into Eq. (8), gives an overall detector maximum gain ($V = 900$ volts) at the CMOS output that is $\sim$104 e^- for each photoelectron produced by the photocathode. This is $\sim$400 DN at the ADC output for each photoevent.

CMOS Characteristics The CMOS detectors operate in correlated double sampling/ non-destructive read mode CDS/NDR (Sect. 5.3), which eliminates fixed pattern offsets, reset (kTC) noise, and lag at the expense of increasing the readout noise by $\sqrt{2}$. In this configuration only dark current noise and readout noise persist. These were measured over a broad temperature range (-40 °C to $+20$ °C) during unit-level testing. Both detectors have nearly identical mean thermal response described by $DN = 1.29 * t_{int} * \exp^{0.088T}$ where DN is the average dark signal data number accumulated during integration time t_{int} and T is the temperature in °C. Dark signal noise is the square root of the number of signal electrons collected during an integration period converted to DN. For the IUVS detectors the gain is 0.04 DN per electron (Sect. 5.3) and the $\sigma(DN) = \sqrt{t_{int}} * 0.23 \exp^{0.044T}$. Read noise, which is essentially independent of temperature, is 2.9 DN for CDS/NDR.

The IUVS thermal subsystem is designed to maintain CMOS detector temperatures below -20 °C throughout the orbital mission. At these temperatures the average dark signal rate is 0.22 DNsec^{-1} per pixel and typical dark signals vary from 0.44 DN per pixel for limb altitude profiles where the integration period is 2 sec to 13.3 DN per pixel for apoapsis images where the integration period is 60 sec. Dark signal noise values for these two integration periods are 0.13 DN and 0.74 DN, respectively.

Full well depth for the IUVS detectors is $\sim 10^5$ electrons corresponding to a typical amplitude of 1.5 volts on the column amplifiers. When the number of electrons accumulated in an individual pixel is less than 8×10^4, the output gain is 15 μV per electron (0.04 DN per electron). Above this level the output gain rapidly declines; therefore IUVS intensifier

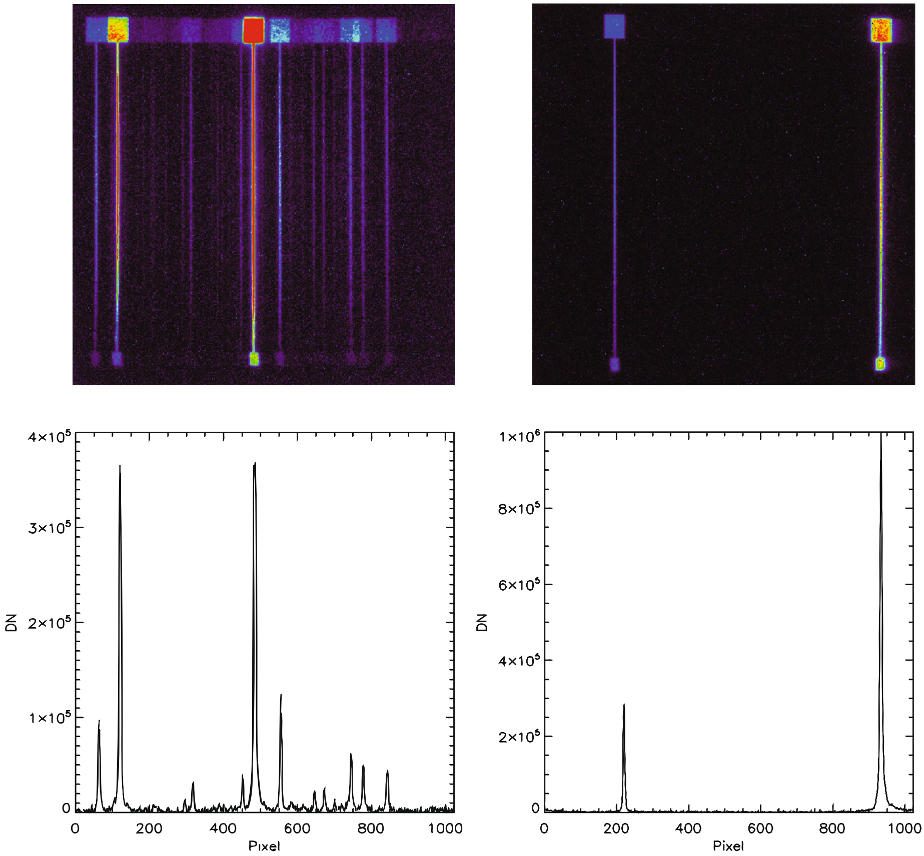

Fig. 24 Standard spatial spectral images for FUV (*top left panel*) and MUV (*top right panel*) have wavelength increasing from *left* to *right* and have the large keyhole at the *top of the image*. Pixel $(0, 0)$ for each image is in its *lower left corner*. Slit images are parallel to the APP $\boldsymbol{j}$ axis with the large aperture pointing in the $-\boldsymbol{i}$ direction. The *bottom panels* are line plots obtained by summing rows 460–560 of each detector

gain levels and integration times are designed maintain output voltages <1.2 v. Not all of this capacity is available for signal electrons because the voltage bias level for some individual pixel amplifiers can be negative by up to 0.5 mvolts corresponding to ~350 DN. This must be accommodated by applying a zero-signal bias to the detector ADC input in order to avoid negative values that are set to 0 in the black images that are acquired as the first step in the CDS/NDR readout mode that is used for all IUVS images. Thus the maximum electron signal level for IUVS is $\sim 7.13 \times 10^4$ electrons (3750 DN).

6.2.3 Wavelength Scale and Focal Plane Distortion

Normal Mode Wavelength Scale The normal mode wavelength scales for the two detectors were measured using spectra from a microwave discharge lamp that was equipped with a mercury bulb and used to illuminate a white reflectance screen located near the telescope nadir aperture. This arrangement filled both the entrance pupil and spectrograph field of view. The telescope cavity and spectrograph were purged with N_2 allowing the radiation from the mercury resonance line located at 184.9 nm to traverse the system. Figure 24 shows

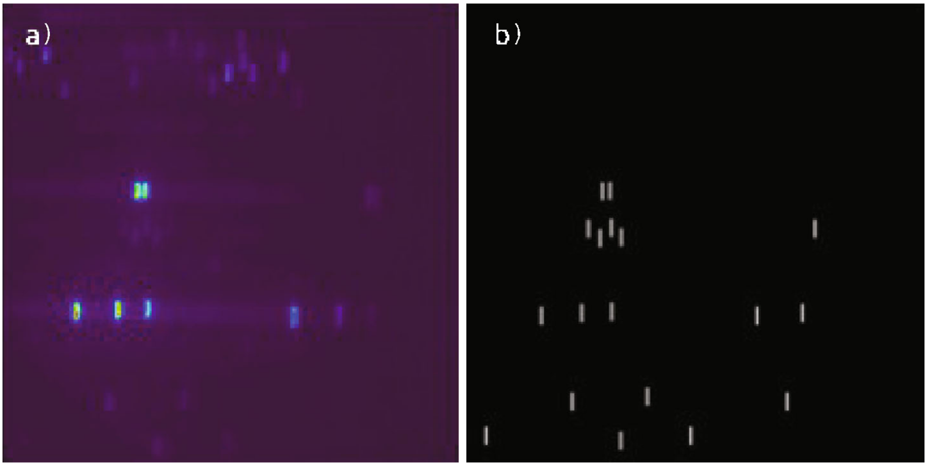

Fig. 25 Echelle image of an $N + N_2$ emission spectrum obtained during instrument calibration using a lamp that only fills 1 mm of the 3-mm-tall echelle entrance slit. The *left panel* is the raw FUV image. Atomic emission features appear in the lower 60 % of the image. Emissions from the Lyman-Birge-Hopfield system of N_2 dominate the upper 20 % of the image. The brightest emissions arise from NI 124.318 nm and 124.331 nm followed by NI 119.955, 120.022, 120.720 nm. The *right panel* is a model of IUVS echelle mode for atomic N

an example of images obtained from this experiment. The upper left and right panels are raw images from the MUV and FUV detectors, respectively, recorded using CDS/NDR. Lower panels show line plots obtained by summing rows 460–560 of the detector images.

The wavelength scale for column N of the detector, $\lambda(N)$, is determined from Eq. (1) with α fixed and β calculated from Eq. (12) with $\Delta \sim 0.0234$ mm and with $\beta_c \sim 8.8°$ for FUV detector and $\beta_c \sim 8.0°$ for the MUV detector, respectively,

$$\beta_N = \beta_c + \tan^{-1}\big((N - 511.5) \cdot \Delta / F\big). \tag{12}$$

In practice $\lambda(N)$ can be adequately approximated by a simple quadratic,

$$\lambda = \lambda_0 + a_\lambda \cdot N + b_\lambda \cdot N^2, \tag{13}$$

which reproduces the solution to Eqs. (1) and (12) to better than $\pm 0.02 \cdot a_\lambda$.

Gaussians were fit to the isolated lines in the plots in the lower left panel of Fig. 24 for MUV and the central-wavelength parameters from those fits were used as estimates of line centers. These were fit to Eq. (13) using a standard least squares algorithm resulting in $l_0 = 174.63$, $a_l = 0.16215$, and $b_l = 2.4201 \times 10^{-6}$. These values provide in a nominal spectral coverage and dispersion for the central 100 rows of the images shown in Fig. 24 of 174.6–343.0 nm with an average 0.1646 nm per pixel (7.017 nm/mm) spacing. The same approach was used for FUV except only two lines are available (253.6 nm in 1st order and 184.9 nm in 2nd order) so only the coverage, 109–192 nm, and average spacing of 0.0814 nm per pixel (3.47 nm/mm) are determined from these data. Inserting the dispersion values into Eq. (3) yields a value for the grating spacing, $d^{-1} = 286.0$ g/mm with $f = 495.1$ mm. This groove spacing is significantly different from the $d^{-1} = 276.0$ g/mm specific in the purchase order to Jobin Yvon. The origin of this discrepancy has not been identified.

Echelle Mode Wavelength Scale The IUVS employs the combination of a short entrance slit (3 mm tall in echelle mode compared to 22 mm tall in normal mode, Sect. 5.4.3) and a MgF_2 cross disperser prism, located directly in front of the grating, to spatially separates overlapping grating orders. The result is a two dimensional spectral image or echellegram. The left panel in Fig. 25 shows an example of an echellegram of $N + N_2$ obtained during ground calibration using a lamp that filled only 1 mm of the 3 mm tall slit. The spectrum consists of isolated atomic features over approximately 70 % of the wavelength range. Emissions from the Lyman-Birge-Hopfield system are evident for wavelengths greater ~123 nm. The pattern is shifted left by ~250 pixels relative to the simulation shown in Fig. 15 to account for an adjustment to spectrograph geometry, which was made during instrument design and fabrication (see Sect. 6.2.1). The right panel is a model of the echelle mode for atomic N, which uses a line list from the NIST atomic database, that predicts the location of the brightest features in the echelle spectrum using the grating equation and the dispersion relation for the MgF_2 prism (Sect. 5.2.3).

In contrast to normal mode, the echelle mode wavelength scale cannot be represented by a simple polynomial. Instead, the wavelength associated with each pixel must be specified using the prism equation for its row number and the grating equation for its column. For a thin prism with apex angle A, the difference in deviation angle for light with wavelength λ and wavelength λ_0 traversing the prism is related to the index of refraction by the equation $\Delta\theta = A \cdot (n(\lambda) - n(\lambda_0))$. In IUVS the echelle grating is tipped so that light from the center of the entrance slit with wavelength $\lambda_0 = 121.5$ nm impinges upon it with $\gamma = 0$ (Eq. (1)). This beam is diffracted by the echelle and emerges undeviated in the cross-dispersion dimension after a second pass through the prism. All other wavelengths impinge upon the echelle at angles $\gamma_c = \Delta\theta$ and deviated by $2\gamma_c = 2\Delta\theta$ after traversing the prism twice. The number for each row of the detector is related to wavelength λ by

$$2 \cdot \gamma_c = \tan^{-1}\bigl((N - 511.5) \cdot \Delta/F\bigr) \tag{14}$$

$$\gamma_c = A \cdot \bigl(n(\lambda) - n(\lambda_0)\bigr) \tag{15}$$

Similar to the normal mode, the grating equation relates wavelength to column position through Eqs. (1) and (12). These results relate detector position to wavelength for light originating from the spectrograph slit center. For heights, h, above and below the slit

$$2 \cdot \gamma - h/F = \tan^{-1}\bigl((N - 511.5) \cdot \Delta/F\bigr) \tag{16}$$

$$\gamma = A \cdot \bigl(n(\lambda) - n(\lambda_0)\bigr) + h/F \tag{17}$$

where $-1.5 \text{ mm} \le h \le 1.5$ mm.

Focal Plane Distortion The fiber optic couplers in the two detectors that connect the output of the intensifiers to the CMOS arrays are fabricated from thick (approximately 20 mm long) faceplates that are drawn to form tapers. This process introduces distortion in the faceplates and the 24 mm square focal planes at their inputs map to trapezoids at their outputs. Thus, each row of the CMOS arrays has a different wavelength scale.

We used images shown in Fig. 24 to measure distortion by fitting Gaussians to the emission lines in 8 individual spectra made by summing 100 rows at a time beginning with rows 200 ± 50 and ending with rows 900 ± 50. The results indicate that the distortion is not uniform. For the MUV detector, slit images at the longest wavelengths are twisted clockwise by 3 pixels while those at the shortest wavelengths are twisted counter clockwise by 1 pixel. For the FUV detector, slit images at the longest wavelengths are twisted counterclockwise by 2 pixels while those at the shortest wavelengths are aligned with the detector column. Thus, using the wavelength scale derived from the central rows of the detector can lead to errors of up to 1 pixel at the top and bottom of the MUV detector and slightly less than 1 pixel for the FUV detector. Focal plane distortion has only a small effect on echelle mode because slit images for individual spectral features are ∼3 mm tall.

The values of λ_0 determined for the images in Fig. 24 are 108.91 nm and 174.56 nm for FUV and MUV, respectively. These values can change by up to ∼±0.8 nm for FUV and ∼±1.6 nm for MUV after a GFM cycle has moved the normal incidence grating out of and back into the collimator beam (Sect. 5.4.3). It is possible that the magnitudes of these displacements will decrease with repeated actuation of the GFM during orbit.

6.2.4 Line Spread Function and Spectroscopic Resolution

Normal Mode The top panel in Fig. 26 shows a 41 × 41 pixel window from an image of the system PSF near the center of the detector field of view, which was obtained using a collimator equipped with a scanning grating monochromator to produce a simulated star source with an angular size 0f 0.2 mrad at a single isolated wavelength. Although its core is rotationally symmetric, the image displays wings that extend along both the dispersion and cross-dispersion axes.

The black curve in the bottom panel shows the line spread function (LSF) in the dispersion direction, which was constructed from the sum of all the rows in the top panel image. Red and blue curves show the best-fit Gaussian and Voigt (the convolution of a Gaussian and a Lorentzian function) profiles, respectively. Whereas the FWHM derived for both fits is approximately 6 pixels, the Voigt functional form is clearly required to fit the far wings of the PSF.

Although the exact origin of the PSF wings is uncertain, several factors are likely to contribute to them. In the cross dispersion direction the beam splitter acts as a coarse grating. The beam splitter pattern is 2 mm tall (1.5 mm reflective and 0.5 mm transmissive) and light from the camera mirror illuminates approximately 10 cycles of this pattern as it approaches the focal plane. The resulting diffraction/interference pattern has an envelop that is well approximated by a Gaussian function with FWHM ∼0.06 mm for MUV and FWHM ∼0.01 mm for FUV, respectively. This effect is not large enough to account for the measured profile. Rough grating grooves and ordinary grating scatter can also lead to broad wings on the grating distribution function, which would affect the PSF in the dispersion direction. This usually results in light scattering over large angles, which is not the effect observed here. Mid-frequency wave-front errors (MFWFE) introduced by zonal polishing of the toroidal camera mirror can also contribute. Finally, some researchers have reported 'halos' around point-source images obtained with intensified CMOS detectors (Ren et al. 2014) Unlike the '+' pattern observed here, both MFWFEs and detector halos are rotationally symmetric.

We adopted the FWHM of the emission lines shown in the top panels of Fig. 24 as the measure of the instrument spectral resolution for an extended source that covers the entire spectrograph entrance slit width. Figure 27 summarizes the performance using FWHM values determined from the 8 equally spaced spectra in the distortion analysis. When combined with the dispersion, these results indicate that the MUV spectral resolution varies from ∼0.82 nm to ∼1.11 nm (MUV uses the left 24 mm of the focal plane) across the focal plane. The FUV spectral resolution varies from ∼0.42 nm to ∼0.63 nm.

These are slightly larger than predicted by the optical model (Fig. 12) with a maximum value of 0.18 mm here compared to 0.16 mm for the model. Figure 27 also reveals that the morphology of the FWHM contours in the as-built instrument, which shows a minimum near the center of the bottom row, differs significantly from that of the model, which shows

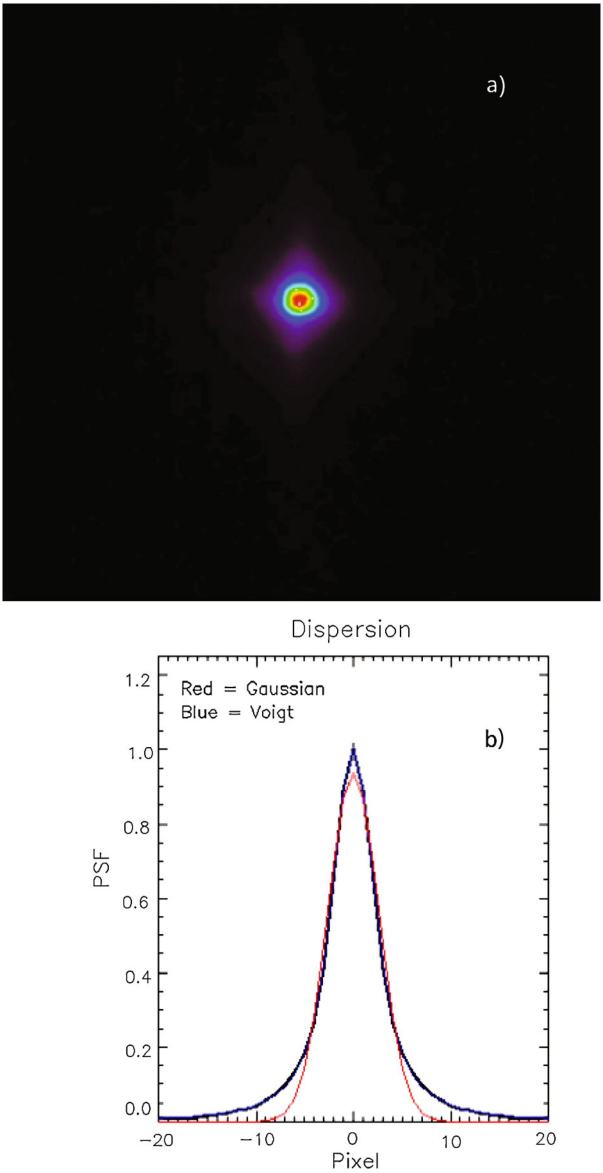

Fig. 26 The *top panel* is a 41-pixel square image of the imaging point spread function (PSF). The *black curve in the bottom panel* is the line spread function (LSF), which was constructed by summing all the rows of the image in the *top panel*. *Red* and *blue* curves are best-fit profiles using a Gaussian function (*red*) and a Voigt function (*blue*)

contours that are nearly uniform in dispersion and increase both above and below the central row. It is possible that the asymmetry observed here is a result of distortion introduced by one or both of the three-point mounts holding the collimator and camera mirrors.

Echelle Mode We estimated the echelle mode line spread function in the dispersion direction for a filled entrance slit using a line plot extracted from the image shown in the left panel of Fig. 25. The left panel of Fig. 28 shows the spectral plot for orders 350 and 351, which was obtained by summing rows 300 through 400 of the image in Fig. 25. There is clear evidence for a broad continuous background that peaks near pixel 250 (see also the

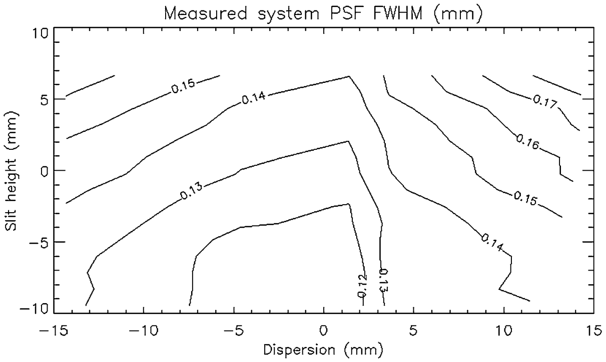

Fig. 27 The imaging point spread function for the spectrograph when the entrance slit is uniformly illuminated. When combined with the system dispersion the resulting spectral resolution varies across the focal plane from ∼0.82 nm to ∼1.11 nm for MUV and from ∼0.42 nm to ∼0.63 nm for FUV

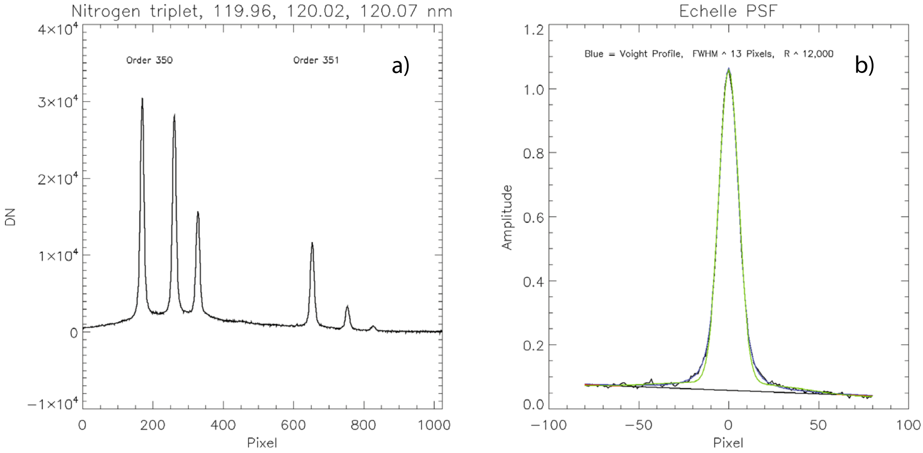

Fig. 28 The *left panel* is a line plot of orders 350 and 351 produced by summing rows 300–400 of the image in the left panel of Fig. 25. The *right plot* shows Gaussian (*green*) and Voigt (*blue*) fits to the profile centered near pixel 650

image in the left panel of Fig. 23). This is most likely due to grating scattered light, which is much stronger for echelles than for typical normal incidence gratings (Content et al. 1996). Gaussian (green) and Voigt (blue) fits to the profile center near pixel 650 are shown in the right panel of Fig. 28. These results show that a Voigt profile more accurately represents the profile than a Gaussian, which is consistent with the normal mode profile.

Whereas the FWHM of the normal mode profile in the as built instrument is comparable to the FWHM obtained from ray trace modeling (paragraph "Normal Mode Wavelength Scale"), the FWHM of the echelle profile is 50 % larger than that of the model profile prediction. The source of this discrepancy is not understood. Referring to Eq. (4), the linear dispersion at hydrogen Lyman alpha (121.567 nm) is 0.0309 nm/mm ($n = 346$ and $\beta = 76.25°$) and spectral resolution for the measured profile is $\Delta\lambda = 9.43 \times 10^{-3}$ nm ($\Delta w = 13$ pixels $= 0.305$ mm) or $R = \lambda/\Delta\lambda = 12{,}900$. This compares to 19,000 inferred from the raytrace model.

The deuterium Lyman alpha line center, at 121.534 nm, is displaced by 0.033 nm (1.07 mm = 45.6 pixels) relative to its hydrogen counterpart and is therefore well resolved, even at $R = 12{,}000$. On the other hand, the intensity in wings of the hydrogen emission line 45 pixels from line center is approximately 1 % of the peak emission and this is likely the limiting factor for detecting weak D emission from the Mars atmosphere. (Note that the additional background present in the profile shown in the right panel of Fig. 28 arises from scattering of the three bright emissions in order 350.) A similar background should not be present in the Mars data because H dominates all other emissions by a factor of 100 or greater. Thus background observed at the D line wavelength is expected to arise from the nearby H line only and is expected to show a level approximately equal to 1 % of the peak of the H line.

6.2.5 Radiometric Sensitivity

Normal Mode IUVS normal-mode radiometric sensitivity was measured using both detector standards (comparison of instrument response to that from a calibrated photodiode) and irradiance standards (calibrated lamps). Both approaches are traceable to National Institute of Standards and Technology (NIST) standards.

In the former calibration approach we used a vacuum facility equipped with a 2.3-m-focal-length collimator that had a scanning monochromator positioned at its focal plane. The monochromator's exit slit was masked to 1 mm in height and the slit was adjusted to be less than 0.2 mm wide so that beam of light exiting the collimator had less than a 0.2 milliradian angular extent. A hollow cathode lamp using flowing H_2, N_2, O_2, and CO_2 was placed at the entrance slit provided spectra with both molecular emissions and isolated atomic emissions. A pair of photomultiplier tubes (PMTs) with pulse-amplifier-discriminators and 2.54-mm-square apertures were placed on a translation stage in the vacuum chamber and coaligned to the IUVS. One of these was equipped with a CsI photocathode and a MgF_2 window for FUV calibrations and the other with a CsTe photocathode and a fused silica window for MUV calibrations. The PMTs' quantum efficiencies were determined as a function of wavelength by comparing their outputs to a photodiode whose absolute quantum efficiency as a function of wavelength was measured by NIST (Canfield et al. 1973). This allowed us to determine a map of input beam irradiance (photons $\mathrm{cm}^{-2}\,\mathrm{sec}^{-1}$) as a function of position within the vacuum chamber by scanning the two PMTs in a raster pattern and measuring their outputs. IUVS responsivity, $R(\lambda_j, \theta_k)$ ($R = T_{Optics} \cdot Qe_{Pc} \cdot G_{Det} \cdot G_{ADC}$) was determined at 20 discrete wavelengths and 7 heights along the slit. A measurement sequence for each wavelength and angle began setting the monochromator to an isolated atomic emission line and mapping the beam with the appropriate PMT. Once map was complete, the PMT was placed in the center of the raster and its count rate was recorded. Next the PMT was translated aside and the IUVS placed at the center of the raster and rotated in elevation to the measurement angle, θ_k, where the DN rate was measured. Finally the PMT was reinserted and its count rate was measured for a second time to determine lamp drift. (No more than a few percent drift was ever observed during a measurement sequence). Two separate measurement sequences were performed; one with the monochromator grating grooves parallel to those of IUVS and one with them perpendicular. These were averaged to account for polarization effects that may have been introduced because the monochromator grating acts as a polarizer and the IUVS grating acts as an analyzer. (The effects were only a few percent, probably because the IUVS grating operates very near the Littrow configuration (James & Sternberg 1969).) Care was taken to accurately account for parallax between the PMTs whose apertures were in one plane and the IUVS whose entrance pupil was in another.

The irradiance standards approach is performed at ambient pressure and can only be used for MUV. It employs lamps that have their spectral irradiance (i.e., photons $\mathrm{cm}^{-2}\,\mathrm{sec}^{-1}\,\mathrm{nm}^{-1}$) directly traceable to NIST standard sources. In this approach a calibrated

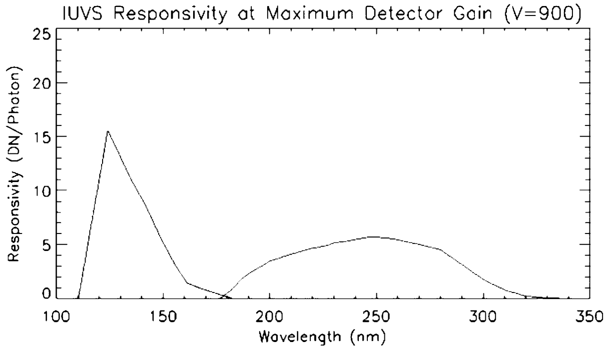

Fig. 29 Responsivity curves for FUV and MUV channels measured before launch. These curves represent the efficiency of the optial-detector system. The signal produced by IUVS for atmosphere emission is the responsivity multiplied by the etendue of the optical system

lamp (irradiance standard) is placed in front of a Spectrolon® screen providing an extended source with a radiance (i.e., photons cm^{-2} sec^{-1} nm^{-1} str^{-1}). Radiance is calculated from the product of lamp irradiance at the screen multiplied by screen reflectance (Georgiev and Butler 2007; Stiegman et al. 1993). When IUVS views a screen that is large enough to fill both its entrance pupil and its field of view the output DN rate from the MUV detector divided by the screen radiance is a direct measure of the quantity $A \cdot \Delta\lambda \cdot R(\lambda_j, \theta_k) \cdot \Omega(\theta_k)$. A measurement sequence includes observations of the screen followed by a dark measurement, obtained by closing the MUV electronic shutter. This is followed by a similar sequence with the screen by a black cloth. Assuming that the cloth reflectance is ≤ 4 % provides a good measure of the ambient backgrounds, which result when light from the lamp is reflected from walls and other objects within the lab into the IUVS field of view. Additionally, measurements are made at a range of instrument-screen separations in order to determine atmospheric absorption, which is small but significant, particularly for wavelengths <240 nm. Both a deuterium lamp (Saunders et al. 1978), which was calibrated for $\lambda > 200$ nm, and an FEL lamp (Walker et al. 1987), which was calibrated for $\lambda > 250$ nm, were used for IUVS. The different spectral properties of these lamps provide insight into the scattered light performance of the IUVS spectrograph.

Figure 29 is a plot of the composite responsivity at FOV center obtained by combining the results from the vacuum calibration (FUV and MUV) with those from the two lamps (MUV only). These are plotted for the respective maximum MCP gains (900 v). We estimate the overall uncertainty in responsivity curves to be ~20 % for FUV and ~15 % for MUV. These estimates will be refined during cruise to Mars using observations of bright ultraviolet-emitting stars, whose irradiances known to 10 % or better (Snow et al. 2013). A detailed analysis of the ground calibration results and their uncertainties and a comparison with cruise measurements will discussed in a subsequent paper.

Photon arrival is a random process described by Poisson statistics. When N_{phot} are the number of signal photons detected during a single integration period, the estimate for the uncertainty in the mean value of N_{phot} for many integration periods, which is often referred to as noise, is $\sqrt{N_{\mathrm{phot}}}$. When an image intensifier is employed in the instrument then the uncertainty is $\sqrt{(E * N_{phot})}$ where E is the intensifier excess noise (Sect. 5.3). The responsivity reported here is the product, $N_{DN} = N_{phot} * G_{Det} * G_{ADC}$; therefore, the uncertainty is $\sqrt{N_{DN}} * \sqrt{(E * G_{Det} * G_{ADC})}$.

During detector calibration we estimated $G_{Det} * G_{ADC}$. This was accomplished by illuminating the detector so that only a few thousand photon events were collected during an integration, determining the centroids of individual events in the output images, and integrating the DNs for the pixels within a 4 × 4 pixel box centered on the centroid. The results are $G_{Det} * G_{ADC} = 390$ DN/phot for MUV and $G_{Det} * G_{ADC} = 460$ DN/phot, both for an MCP voltage of 900 v. (For example, noise $= 30 * \sqrt{N_{DN}}$ and $28 * \sqrt{N_{DN}}$ for FUV and MUV, respectively, when MCP voltage = 900 v.) These values will also be refined in flight using stars.

The signal produced by IUVS for atmosphere emission is the responsivity multiplied by the etendue of the optical system. For example the etendue for a normal-mode observation that includes the entire length of the airglow slit (0.1 mm wide × 19.8 mm tall) is $A_S * A_T / F_T^2 = 0.01 * 1.98 * 1.33 * 2/100 = 5.28 \times 10^{-4}$ cm^2 steradian, where A_S and A_T are the slit and telescope areas and F_T is the telescope focal length. If the radiance at the aperture for 121.567 nm is measured in kilorayleighs (1 kr $= 10^9$ photons/sec emitted into 4π steradians), then the instrument sensitivity is 5.5×10^5 DN/sec/kr.

Echelle Mode The echelle mode responsivity was estimated before calibration to be $0.36 * 0.56 * 0.5 \sim 0.1$ of the normal mode value. This is based on the echelle spectrograph beam filling factor of 0.36. (The effective echelle grating width is $W * \cos(\beta) = 24.1$ mm compared to $w = 66.7$ mm for the normal mode (Bottema 1981), the transmission of the MgF$_2$ prism, which when used in double pass is $0.75^2 = 0.56$, and the relative echelle grating/normal grating groove efficiency of 0.5 (Content et al. 1996).) This estimate was validated at 121.567 nm by taking images in normal and echelle modes while the IUVS viewed the vacuum collimator with the monochromator set to transmit H Lyman alpha emission from its hollow cathode lamp. The ratio of the total DNs within each of the two measured profiles was Total(Echelle)/Total(Normal mode) ~0.096. Thus responsivity of the echelle mode is ~1.3 DN/photon for 121.567 nm. The echelle mode signal for atmosphere emission is 66 times smaller because the etendue and optical throughput are 6.6 and 10 times less, respectively, than normal mode.

7 Conclusion

IUVS is one of three science instrument suites aboard the MAVEN spacecraft, which was launched on November 18, 2013, on its way to a one Earth-year orbital mission around Mars. The instrument supports two spectroscopic modes. IUVS incorporates innovative approaches to package-proven optical designs and detector technologies into an instrument that must provide a wide range of measurement capability. It will provide important measurements that will address MAVEN scientific objectives related to process taking place in the Mars upper atmosphere today and its evolution over geologic time.

Acknowledgements More than three-dozen managers, scientists, engineers, technicians, and instrument makers at the Laboratory for Atmospheric and Space Physics contributed to the design, fabrication, and test of IUVS. Their expertise, dedication, and hard work transformed the IUVS concept into a world-class scientific instrument. We also thank two anonymous referees whose insightful comments and detailed edits significantly improved the quality of this paper. This work was supported by the National Aeronautics and Space Administration's Mars Scout Program through contracts to the University of Colorado.

References

C.A. Barth, Annu. Rev. Earth Planet. Sci. **2**, 333 (1974)
C.A. Barth, M.L. Dick, Icarus **22**, 205 (1974)

C.A. Barth, C.W. Hord, J.B. Pearce, K.K. Kelly, G.P. Anderson, A.I. Stewart, J. Geophys. Res. **76**, 2213 (1971)
C.A. Barth, C.W. Hord, A.I. Stewart, A.L. Lane, Science **175**, 309 (1972a)
C.A. Barth, A.I. Stewart, C.W. Hord, A.L. Lane, Icarus **17**, 457 (1972b)
J.-L. Bertaux, F. Leblanc, S. Perrier, E. Quemerais, O. Korablev, E. Dimarellis, A. Reberac, F. Forget, P.C. Simon, S.A. Stern, B. Sandel, Science **307**, 566 (2005a)
J.-L. Bertaux, F. Leblanc, O. Witasse, E. Quemerais, J. Lilensten, S.A. Stern, B. Sandel, O. Korablev, Nature **435**, 790 (2005b)
J.-L. Bertaux, O. Korablev, S. Perrier, E. Quémerais, F. Montmessin, F. Leblanc, S. Lebonnois, P. Rannou, F. Lefèvre, F. Forget, A. Fedorova, E. Dimarellis, A. Reberac, D. Fonteyn, J.Y. Chaufray, S. Guibert, J. Geophys. Res. Planets **111**, E10S90 (2006)
M. Bottema, Appl. Opt. **20**, 528 (1981)
L.R. Canfield, R.G. Johnston, R.P. Madden, Appl. Opt. **12**, 1611 (1973)
M.S. Chaffin, J.-Y. Chaufray, I. Stewart, F. Montmessin, N.M. Schneider, J.-L. Bertaux, Geophys. Res. Lett. **41**, 314 (2014)
J.W. Chamberlain, Planet. Space Sci. **11**, 901 (1963)
J.Y. Chaufray, J.L. Bertaux, F. Leblanc, E. Quémerais, Icarus **195**, 598 (2008)
D.A. Content, R.A. Boucarut, C.W. Bowers, T.J. Madison, G.A. Wright, D.J. Lindler, L.K. Huang, B.P. Puc, C. Standley, T.A. Norton, SPIE Proc. **2807**, 267–278 (1996)
M. Czerny, A.F. Turner, Z. Phys. **61**, 792 (1930)
A. De Groof, D. Berghmans, B. Nicula, J.-P. Halain, J.-M. Defise, T. Thibert, U. Schühle, Sol. Phys. **249**, 147 (2008)
P.D. Feldman, E.B. Burgh, S.T. Durrance, A.F. Davidsen, Astrophys. J. **538**, 395 (2000)
P.D. Feldman, A.J. Steffl, J.W. Parker, M.F. A'Hearn, J.-L. Bertaux, S. Alan Stern, H.A. Weaver, D.C. Slater, M. Versteeg, H.B. Throop, N.J. Cunningham, L.M. Feaga, Icarus **214**, 394 (2011)
J.L. Fox, A.B. Hać, Icarus **228**, 375 (2014)
G.T. Georgiev, J.J. Butler, Appl. Opt. **46**, 7892 (2007)
G.R. Harrison, J. Opt. Soc. Am. **39**, 522 (1949)
C.W. Hord, W.E. McClintock, A.I.F. Stewart, C.A. Barth, L.W. Esposito, G.E. Thomas, B.R. Sandel, D.M. Hunten, A.L. Broadfoot, D.E. Shemansky, J.M. Ajello, A.L. Lane, R.A. West, Space Sci. Rev. **60**, 503 (1992)
James & Sternberg, Design of Optical Spectrometers (1969)
V.A. Krasnopolsky, P.D. Feldman, Science **294**, 1914 (2001)
V.A. Krasnopolsky, P.D. Feldman, Icarus **160**, 86 (2002)
V.A. Krasnopolsky, G.R. Gladstone, J. Geophys. Res. Space Phys. **101**, 15765 (1996)
V.A. Krasnopolsky, G.R. Gladstone, Icarus **176**, 395 (2005)
V.A. Krasnopolsky, M.J. Mumma, G.R. Gladstone, Science **280**, 1576 (1998)
F. Leblanc, J.Y. Chaufray, J. Lilensten, O. Witasse, J.-L. Bertaux, J. Geophys. Res. Planets **111**, E09S11 (2006)
F. Leblanc, J.Y. Chaufray, J.L. Bertaux, Geophys. Res. Lett. **34**, L02206 (2007)
F. Leblanc, O. Witasse, J. Lilensten, R.A. Frahm, A. Safaenili, D.A. Brain, J. Mouginot, H. Nilsson, Y. Futaana, J. Halekas, M. Holmström, J.L. Bertaux, J.D. Winningham, W. Kofman, R. Lundin, J. Geophys. Res. Space Phys. **113**, A08311 (2008)
L. Maltagliati, F. Montmessin, A. Fedorova, O. Korablev, F. Forget, J.-L. Bertaux, Science **333**, 1868 (2011)
W.E. McClintock, M.R. Lankton, Space Sci. Rev. **131**, 481 (2007)
M.B. McElroy, T.M. Donahue, Science **177**, 986 (1972)
F. Montmessin, J.-L. Bertaux, E. Quémerais, O. Korablev, P. Rannou, F. Forget, S. Perrier, D. Fussen, S. Lebonnois, A. Rébérac, E. Dimarellis, Icarus **183**, 403 (2006)
S. Perrier, J.L. Bertaux, F. Lefèvre, S. Lebonnois, O. Korablev, A. Fedorova, F. Montmessin, J. Geophys. Res. Planets **111**, E09S06 (2006)
E. Quémerais, J.-L. Bertaux, O. Korablev, E. Dimarellis, C. Cot, B.R. Sandel, D. Fussen, J. Geophys. Res. Planets **111**, E09S04 (2006)
L. Ren, F. Shi, H. Guo, D. Cui, Y. Qian, H. Wang, B. Chang, in *Unifying Electr. Eng. Electron. Eng.*, ed. by S. Xing, S. Chen, Z. Wei, J. Xia (Springer, New York, 2014), pp. 1109–1116
B.R. Sandel, A.L. Broadfoot, Appl. Opt. **25**, 4135 (1986)
R.D. Saunders, W.R. Ott, J.M. Bridges, Appl. Opt. **17**, 593 (1978)
D.J. Schroeder, *Astronomical Optics* (Academic Press, San Diego, 2000)
M. Snow, A. Reberac, E. Quémerais, J. Clarke, W.E. McClintock, T.N. Woods, in *Cross-Calibration Far UV Spectra Sol. Syst. Objects Heliosphere*, ed. by E. Quémerais, M. Snow, R.-M. Bonnet (Springer, New York, 2013), pp. 191–226
A.I. Stewart, J. Geophys. Res. **77**, 54 (1972)

A.I. Stewart, C.A. Barth, C.W. Hord, A.L. Lane, Icarus **17**, 469 (1972)
A.E. Stiegman, C.J. Bruegge, A.W. Springsteen, Opt. Eng. **32**, 799 (1993)
J.E. Volder, IRE Trans. Electron. Comput. **EC-8**, 330 (1959)
J.H. Walker, R.D. Saunders, A.T. Hattenburg, Metrologia **24**, 79 (1987)
T.N. Woods, R.T. Wrigley, G.J. Rottman, R.E. Haring, Appl. Opt. **33**, 4273 (1994)